Toward Predictable Tendon Driven Soft Robots: Methods in Friction, Design, and Simulation

Christopher-Denny Matte

A Thesis

In the Department

of

Mechanical, Industrial and Aerospace Engineering

Presented in Partial Fulfillment of the Requirements

for the Doctorate in Mechanical Engineering at

Concordia University

Montreal, Quebec, Canada

September 2025

CONCORDIA UNIVERSITY

SCHOOL OF GRADUATE STUDIES

This is to certify that the thesis prepared

By: Christopher-Denny Matte

Entitled: Toward Predictable Tendon Driven Soft Robots: Methods in Friction, Design, and Simulation

and submitted in partial fulfillment of the requirements for the degree of

DOCTOR OF PHILOSOPHY Mechanical, Industrial and Aerospace Engineering

complies with the regulations of the University and meets the accepted standards with respect to originality and quality.
Signed by the Final Examining Committee:

Dr. Nematollaah Shiri Chair

Dr. Yayue Pan External Examiner

Dr. Hang Xu Arms-Length Examiner

Dr. Brandon Gordon Examiner

Dr. Wen-Fang Xie Examiner

Dr. Tsz-Ho Kwok Thesis Supervisor

Approved by: _____

Date: September 1st 2025 _____

Dean of Faculty

Abstract

Toward Predictable Tendon Driven Soft Robots: Methods in Friction, Design, and Simulation

Christopher-Denny Matte, Ph.D.

Concordia University, 2025

Soft robots have unique properties such as inherent compliance, safety, and adaptability, which make them attractive for applications in unstructured and human-centric environments. However, their nonlinear mechanical properties and geometric complexity pose significant challenges in modelling, design, and simulation. In addition, the unique qualities of cable-driven grippers which mimic muscle tendons, provide high force density and greater control, bring their own challenges.

This thesis addresses three critical interrelated challenges which limit the scalability and reliability of tendon-driven soft robotic grippers: (1) the lack of accurate cable friction modelling for elastic surface contacts, (2) the cost and inefficiency of the design process for task-specific grippers, and (3) the absence of real-time simulation tools that accommodate hyperelastic and multi-material behaviour.

First, a novel friction model is proposed that captures the asperity behaviour between cables and elastic surfaces. Unlike existing friction models developed for rigid systems, this formulation accounts for deformation-dependent force transmission and can be calibrated with as few as nine data points. When validated experimentally, the model reduced tip prediction error from 16.1% (baseline) to 2.8% for a soft robotic finger with three joints.

Second, a grasp-based product classification framework is introduced. The framework maps food items to a small set of human-inspired grasp types. This classification supports a modular and reconfigurable gripper design strategy that balances versatility with task-specific performance. A streamlined design pipeline integrates human demonstration data, kinematic modelling, stiffness and cable placement optimization to rapidly generate custom gripper configurations. The resulting modular gripper was

validated across 15 diverse food items, achieving trajectory tracking accuracy exceeding 97%, with a reconfiguration time under five minutes and full fabrication cycles under 24 hours.

Third, to support simulation-informed design and control, a novel geometry-based simulation framework is developed to efficiently model nonlinear, hyperelastic deformations. By embedding strain energy-dependent stiffness into element-wise parameters, the approach dynamically captures material behaviour without updating the global stiffness matrix, thereby maintaining the computational speed advantage geometry-based solvers have. This method enables rapid simulation of complex geometries with arbitrary amounts of materials. Thus, addressing current limitations which restrict existing geometry-based methods to two linear materials.

Collectively, the work presented in this thesis contributes new theoretical models, computational methods, and experimental frameworks that enable faster, more reliable, and more adaptable design of soft robotic grippers. These contributions address key bottlenecks in friction characterization, design scalability, and material simulation, and provide a pathway toward broader industrial adoption of soft robotics.

Acknowledgements

First and foremost I would like to thank my supervisor Dr. Tsz-Ho Kwok whose guidance, knowledge and genuine desire for his students to be the best versions of themselves has greatly impacted the individual I am today. This has been a formative journey in the world of academia and the pursuit of new knowledge and I am grateful for the diverse opportunities and experiences. The Design and Additive Manufacturing (DAM) Lab has been an enriching environment throughout my graduate studies and I thank all those who shared that journey, exchanging ideas and honing skills together. I would also like to thank Chantal Simard, Tom Downey and Brad Moffet for their ability to demonstrate early on how fun science, physics, robotics and teaching can be. I could not have achieved this without the support of my parents and my friends through the non-linear journey that is a doctorate degree. Finally I would like to thank my partner who worked alongside me on the late nights and helped keep me grounded.

Contents

List of Figures

List of Tables

Chapter 1

Introduction

1.1 Background

As automation continues to expand across various industries, robotic systems must evolve to handle an increasingly diverse array of objects. A critical component enabling these interactions is the end-effector, the interface between the robot and its environment. End-effectors are specifically designed for tasks such as welding, inspection, and, most commonly, grasping. Grasping mechanisms, or robotic grippers, are widely utilized in industries ranging from agriculture and automotive manufacturing to pharmaceuticals. These applications typically involve securing, manipulating, or transporting objects in pick-and-place operations, which are fundamental in assembly, disassembly, and material handling. Industries such as recycling, where hazardous materials necessitate robotic solutions, and food processing, where hygiene and throughput are paramount, continue to drive advancements in gripper design.

The effectiveness of a robotic gripper is dictated by the specific requirements of its

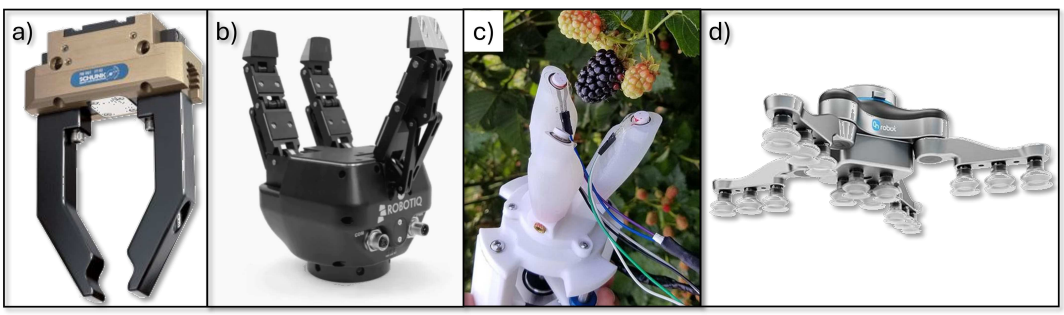

FIGURE 1.1: Different types of robotic grippers: a) Typical rigid jaw gripper by Schunk; b) Compliant rigid gripper by ROBOTIQ; c) Bio-inspired tendon-based soft robotic gripper for blackberry harvesting[1]; d) Suction-based gripper by OnRobot

application, influencing its geometry, actuation mechanism, and material selection. High-load and high-precision applications demand rigid grippers typically made of metal. However, industries that deal with objects of varying size, shape, and material properties prioritize adaptability. In collaborative robotics, where humans and robots share workspaces, safety considerations further impact gripper design, often favouring softer materials that enhance predictability and compliance. For example, the RBO Hand 3, a pneumatically actuated soft robotic gripper, has demonstrated safe and versatile grasping in human-robot collaboration scenarios [2]. Similarly, industries that handle fragile and irregularly shaped objects, such as agriculture and food processing, benefit from grippers with compliant, deformable structures that mitigate the risk of damage.

Rigid grippers, commonly used in industrial pick-and-place applications, rely on precise motion control and force sensing to function effectively (Fig.1.1 a). However, their performance deteriorates in high-mix environments such as prosthetics and food handling, where object variability complicates grasping strategies. Ensuring accurate and reliable manipulation in these environments necessitates extensive sensing and computation, increasing system complexity and reducing operational efficiency. To address these limitations, researchers have explored modifications to rigid grippers by incorporating compliance through underactuated mechanisms (Fig.1.1 b). These designs improve adaptability while maintaining a degree of rigidity for structured tasks. Despite these advancements, rigid grippers still struggle to balance precision, adaptability, and ease of control, particularly in scenarios where object fragility and unpredictability are dominant factors [3].

The food industry exemplifies the challenges of robotic grasping, as robotic adoption has lagged behind sectors such as automotive and electronics manufacturing. Unlike standardized industrial components, food products vary significantly in shape, texture, and mechanical properties, making them difficult to handle with traditional rigid grippers. Soft robotic grippers have demonstrated superior performance in food handling by conforming to objects without requiring precise force control, reducing damage and increasing efficiency [4]. The gripper developed by Gunderman *et al.*[1] for blackberry harvesting, seen in Fig.1.1 c), demonstrates the potential of a tendon-driven soft grippers in adaptive grasping tasks. These grippers have been successfully

deployed for tasks such as gripping delicate fruits, baked goods, and irregularly shaped produce, showcasing their potential to revolutionize automation in this sector.

Beyond food handling, soft robotic grippers have proven valuable in diverse applications requiring compliance and adaptability. In recycling and waste sorting, soft grippers have been used to grasp deformable materials such as plastics and textiles, areas where traditional rigid grippers struggle [5]. Similarly, in the biomedical field, soft grippers have been integrated into minimally invasive surgical systems and prosthetic devices to provide gentle yet secure manipulation of biological tissues [6]. Uniquely, most soft robots achieve movement through distributed actuation within flexible materials [7]. Their ability to deform is directly influenced by their shape and material composition, allowing for tunable motion characteristics. By strategically adjusting geometry or material placement, engineers can program specific movements, enabling innovative robotic designs with enhanced adaptability and functionality.

Since soft robots rely on material compliance to achieve dexterous movement, the choice of actuation method plays a crucial role in their performance. Pneumatics, shape memory alloys, and tendon-driven mechanisms are among the primary means of actuation, each offering distinct advantages. Suction-based end-effectors have been widely adopted due to their simplicity and low cost, yet their effectiveness is limited when handling moist, porous, or irregularly shaped items (Fig.1.1 d). Tendon-driven soft grippers are particularly attractive due to their superior force control, high force density, low noise, and compactness. Unlike pneumatic grippers, which operate in an on-off fashion, tendon-driven systems enable fine-tuned tension regulation, making them more suitable for complex manipulation tasks. This level of control is especially valuable in applications that mix precise deformation and compliance. Tendon driven soft grippers can uniquely leverage biomimicry, the ability to mimic nature, to emulate the gold standard of adaptable grippers, the human hand [3]. As industries increasingly demand manipulators that combine adaptability, precision, and gentle handling, advancing tendon-driven soft robotic grippers becomes essential for unlocking the next generation of versatile, human-like robotic grasping.

1.1.1 Problem statement

Despite their many advantages, soft robotic grippers face significant challenges that hinder their widespread industrial adoption. A primary obstacle is the trade-off between performance and the time and cost required for their design [8]. Unlike rigid robots, which benefit from well-established mathematical frameworks such as Denavit-Hartenberg (DH) parameters for kinematic modelling, soft robots lack a standardized modelling approach. Rigid robotic systems can be systematically designed, analyzed, and controlled using repeatable mathematical tools, enabling efficient validation of preliminary requirements. In contrast, soft robots, characterized by continuous deformable bodies, distributed actuation, and an effectively infinite number of degrees of freedom (DoF), cannot be represented using DH parameters.

As a result, soft robotic systems often rely on simulation-based approaches [9] or data-driven machine-learning techniques [10, 11] to predict their behaviour after fabrication. This reliance limits the ability to develop transferable, repeatable design methodologies, forcing researchers and engineers to depend on trial-and-error processes guided by intuition and experience. Furthermore, without a general mathematical model to describe soft robot deformation, accurately estimating internal forces—particularly in tendon-driven systems where cables interact with elastic surfaces—remains a significant challenge.

1.2 Research Scope and Objectives

This thesis aims to address critical gaps in tendon-driven soft robotic grippers by focusing on three key areas. First, it investigates the complex interactions between tendons and deformable surfaces, a crucial yet under explored aspect of tendon-driven soft robotics. Second, it explores strategies to reduce the reliance on trial-and-error in gripper design. Finally, it seeks to improve the accuracy of simulation methods, enabling more reliable predictive modelling of soft robotic behaviour.

1.2.1 Cable friction

A fundamental challenge in tendon-driven soft robotics lies in accurately modelling how friction develops between tendons and deformable surfaces—especially in the

presence of compliance and surface irregularities. In designing a three-joint finger with uniform closing when actuated by a single cable, the instinctive approach ensures all joints share the same geometry and loading point, as depicted in Fig. 1.2a. This design aims to achieve equal tension at each joint, a notion supported by various kinematic models in existing literature [11, 12, 13]. However, Fig. 1.2e reveals that when the cable is pulled, and the finger closes, the joints closer to the actuation point undergo more significant deformation. Contrary to our intuition, which assumes uniform tension across joints, this outcome challenges the initial design assumption. In my analysis, I identified that the oversight of internal force distribution in models is a crucial factor, particularly the significant impact of friction between elastic surfaces, which cannot be disregarded.

The frictional dynamics of cables play a crucial role in influencing the positioning and response of objects [14, 15]. Despite its significant impact, friction is often overlooked in modelling due to its complexity [9, 12, 16]. In cable-driven soft robotics, where cables interact with elastic surfaces, it becomes imperative to account for cable and surface deformation when analyzing friction behaviour. As three-dimensional (3D) printing gains prominence as a fabrication method for soft robotic applications, various factors such as new geometries, and surface characteristics (including layer lines, finish, and potential print artifacts) substantially influence the frictional behaviour of a cable traversing its surface. The commonly employed Capstan model [17, 18, 19] relates the difference in incoming tension to the outgoing tension based on the deflection or number of cable wraps around an arbitrary cylinder. A more recent model by Heap *et al.* [20] considers the viscoelastic behaviour of the cable and consolidates various findings. Despite the advancements in these models, my preliminary investigation, utilizing a kinematic model incorporating friction, reveals shortcomings in both the Capstan model (Fig. 1.2b) and Heap *et al.*'s model (Fig. 1.2c) in fully capturing the frictional effects present in soft robots.

These models assume the necessity of a normal force for friction to occur, implying zero friction when the angle is zero. However, the high asperity of the cable and the contact surface results in some adhesion forces even when normal forces are negligible. The research question guiding this area of my thesis is: *How to integrate the inherent asperity and elasticity of the contact surface in cable-actuated soft robots into the*

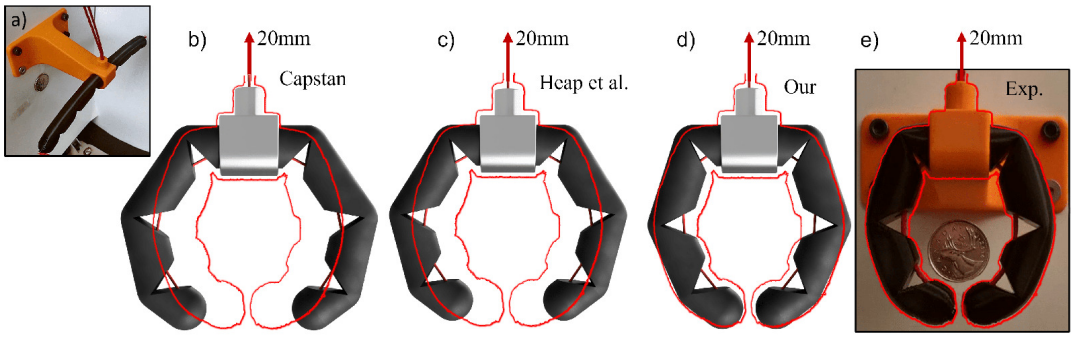

FIGURE 1.2: Effect of friction model on the simulation of a soft robotic gripper. a) 3D printed TPU soft gripper with three joints, b) soft gripper simulated using Capstan friction at 20mm of actuation, c) soft gripper simulated using Heap *et al.'s* friction model at 20mm of actuation, d) soft gripper simulated using my friction model at 20mm of actuation, e) soft gripper at 20mm of actuation.

modelling of friction behaviour?

1.2.2 Design

Design exploration is a foundational challenge in soft robotics, where actuator placement, geometry, and material distribution deeply influence performance. In the absence of robust simulation tools or predictive frameworks, gripper design often depends on iterative trial-and-error, limiting scalability and slowing innovation. This thesis, in part, examines how a grasp-centric, biomimetic approach can streamline design for food-handling applications, where repeatability and adaptability are both critical yet difficult to balance.

Soft robotic grippers for food handling can be broadly categorized into generic and specialized grippers. Generic grippers are designed for versatility, capable of handling a wide range of products without customization [21]. However, their adaptability comes at the cost of precision, making them inadequate for delicate or high-precision tasks. Specialized grippers, on the other hand, can be designed to handle fragile items like eggs and berries, as well as challenging conditions such as sticky, wet, or high-precision operations [1]. While they offer superior performance for specific applications, they come with major drawbacks: high cost, limited adaptability, and inefficiencies in mixed-product environments. In food automation, one of the most pressing challenges is overhead changeover time–the significant effort required to reconfigure robotic grippers when switching between different products. This bottleneck

severely limits automation efficiency and scalability. Worse still, even identical food items can vary in size, ripeness, and stiffness, further complicating the handling process. With the food industry operating on low profit margins, the high cost and lack of adaptability in current robotic grippers make widespread automation economically unfeasible for many manufacturers. Without a breakthrough in flexible, cost-effective gripper technology, the advancement of food automation will remain impeded. There is an urgent need to develop robotic grippers that combine the versatility of generic systems with the precision of specialized design–while remaining affordable and easy to reconfigure.

I observe that, despite the diversity of object shapes, humans rely on a finite set of grasp types. The primary variations arise from differences in applied force and the extent of hand closure required to accommodate the object's size. For instance, the same grasp type can be used to gently hold an egg or firmly grip a hammer. Feix *et al.* [22] identified 17 general human grasp types, though most daily tasks rely on a subset of 6 to 9 common grasps, such as power, pinch, tripod, and lateral grasps. In the food industry, I anticipate that an even smaller subset will suffice, given the repetitive and task-specific nature of food handling. However, a key challenge in industrializing soft robotic grippers is balancing performance with the time and cost involved in their design, primarily due to the reliance on lengthy trial-and-error processes [8]. Moreover, grasping is not solely about achieving a final shape; the motion trajectory leading to the grasp is equally critical, as it directly influences grasp stability, efficiency, and adaptability [23]. Thus, the second research question addressed in this thesis is: *How can we cost-effectively customize and optimize a path-dependent gripper for each grasp-based product mix while maintaining a simple and scalable actuation strategy?*

1.2.3 Simulation

Simulation plays a critical role in reducing the trial-and-error inherent in soft robotic design, yet current tools often struggle to balance speed with the accuracy required for modelling complex, non-linear materials. As soft robots increasingly rely on hyperelastic materials and embedded actuators, the need for real-time, high-fidelity simulations has become urgent.

The Finite Element Method (FEM) has been used for decades to simulate deformations of solids, flows of liquids and gases, as well as thermal responses of systems. The applications also include the simulation of soft robots, surgical processes, and animation. This has allowed medical fields, exploration, and video games to simulate more realistic behaviours and phenomena. Additionally, this has enabled designers to simulate before needing to fabricate, allowing for a more freeform understanding of their tasks and solutions. Current research aims to increase the performance of FEM solvers to allow for realistic deformations at real-time speeds. Current solutions aim to either reduce the computational load by linearizing complex material properties [24, 25] or simplifying the three-dimensional (3D) models [26, 27]. All of these aim to have real-time simulation for their respective applications while maintaining robustness. However, the need for interactive, complex, and non-linear simulation has made current solutions unintuitive or unable to incorporate both accuracy and speed.

New simulation methods have been proposed to increase simulation speed, but at the cost of accuracy, such as position and projection dynamics [28]. These simulations ensure visual plausibility while decreasing computational cost. Dealing directly with nodal displacements instead of classical Newtonian methods limits the number of calculations required. Mostly used in computer graphics, they have also been adapted for engineering practices as well for the simulation of smart materials and more intuitive actuation of soft robots [29, 30].

However, these simulations mainly deal with linear phenomena. Some material's behaviour depends on their deformed state, meaning their properties and relations need to be updated at every time-step to match their current state. Hyperelastic materials are a class of elastomers that exhibit non-linear material properties and rely on their instantaneous rigidity as a function of strain to dictate their stiffness. This directly applies to soft robots as they are mainly made using hyperelastic material such as silicone, rubbers, or 3D printed polymers [31, 32, 33, 34]. This is also true for surgical simulations requiring the modelling of flesh [35]. Their deformation is dictated by the actuation mechanism and the material distribution within the robot. It is currently possible to simulate specific deformations of soft robots given proper constraints and inputs. However, generally, simulations are not fast enough to be all-encompassing or able to interact in real-time. Some methods proposed faster simulation but failed to

depict large deformation accurately or are limited in applications [36].

Recently, Kwok *et al.* [29] proposed using geometry-defined finite elements (GDFE) to express actuations of smart materials in a geometric form. Contrary to traditional FEM, the global matrix in GDFE is not updated during the deformation, which is a key for fast computational speed. This concept was then adapted by Fang *et al.* [30] to show that actuations typically used for soft robots can be treated as changes in geometry. Their work demonstrated the approach could lead to a real-time simulation of soft robots and a significant performance increase over FEA while maintaining the current state-of-the-art stability and speed. Although their work proved that geometry could exhibit the behaviours of two materials simultaneously, it is also the maximum number of materials the method can handle and the property of the materials must be linear. Thus, the current state-of-the-art simulation is still missing the ability to simulate more than two materials as well as hyperelastic materials.

Despite the current limitations, I observed that the method is promising in terms of versatility. It can represent different actuations and material properties by only changing the geometric target shapes. This motivates my research to answer the following research question: *How to express the non-linear material behaviour through the shape functions on a local level, such that the computational speed is not affected?*

1.3 Thesis Structure

By bridging fundamental research with practical applications, this thesis expands the scientific understanding of tendon-driven soft robots and improves their feasibility for industrial deployment, ultimately advancing both the theoretical and applied aspects of soft robotic grippers. The rest of the thesis will be broken down into four main sections. Chapter 2 will discuss works related to soft robots, the modelling of cable friction, on soft robotic grippers, and their simulation. Chapter 3 pertains to the development of a novel friction model between an elastic cable and an elastic surface. While Chapter4 presents a design pipeline for creating soft robotic grippers within the context of the food industry. Chapter 5 will discuss a geometric framework for the simulation of hyperelastic materials. Each chapter is broken down further into their

respective subsections outlining their contributions, methodologies and implementations. Chapter 6 will summarize and elaborate on the future of these works.

Chapter 2

Related Work

2.1 Cable Friction

2.1.1 Modelling of Friction

Amonton's law states that the friction force is proportional to the applied force $F = \mu N$. Bowden *et al.* [37] state that this model is ideal for plastically deforming metals but does not account for changing surface areas and viscoelastic behaviour as seen with cables. In 1951, the power law was introduced to account for the viscoelastic behaviour in the form of $F = \alpha N^n$ [38] and later confirmed by Howell *et al.* in 1953 [39]. n represents the viscoelastic behaviour, and a value of $n = 1$ for a plastic contact is in agreement with Amonton's law. The latter paper gives an approximate range of $0.67 < n < 1$, where a lower value for n means a more elastic contact. In addition, it observes the dependence on the initial loading of the cable and the ratio between the cable radius and the radius of the cylinder. Jung *et al.* [40] proposed a theoretical numerical model with rigidity, non-linear friction, and extensibility and later added the power law friction model [41]. However, this model is complex and requires a 4^{th} order Runge-Kutta approximation. Additionally, obtaining the parameters for the model, such as the Poisson ratio and Young's modulus, can be challenging. Heap *et al.* [20] simplified and experimentally validated the model proposed by Jung *et al.* [41] for a braided line over a metal rod with deflection angles from 16π to 40π (8 to 20 wraps) and loads ranging from $20N$ to $120N$. These ranges are significantly higher than those used in soft robotics and represent a concentric loading case where the pinion is squeezed uniformly. Despite research demonstrating the effects of loading tension and radius ratio between the surface and the cable, the current ASTM standard [42] still

recommends simply using the Capstan model, which only considers cable deflection. Current research indicates that cable deflection, initial loading, radius ratio, and cable speed affect the friction model in some capacity. However, there is limited research on softer frictional surfaces and their effect on cable friction.

2.1.2 Friction in tendon-driven Soft Robots

Salvietty *et al.* [12] chose to ignore friction entirely in their attempt to create a mathematical model for trajectory planning of an underactuated gripper, as it was too complicated to implement. Similarly, in some state-of-the-art FEM simulation methods for soft robots, friction is often omitted, contributing to errors due to uniform bending of joints in cable-driven soft grippers and fingers [16, 9]. However, it is not always possible to limit the effect of friction by incorporating pulleys and minimising the amount of deflection in the cable. Applications such as under-actuated hands require the cable to deflect throughout the actuation while slipping over guides made of metal, plastics, or rubbers [43]. Others, such as continuum robots, require a flexible actuation method to enable their unique deformation, but are greatly affected by the friction behaviour of the cable [13, 44].

Adding to the complexity, 3D printing has become increasingly popular in manufacturing soft robots as the feasibility and diversity of flexible materials continue to expand. As soft robot deformation is directly linked to its geometry, 3D printing allows for more complex designs and more complex actuations. Within this space, PLA is widely considered one of the most popular 3D printing plastics for the fused filament manufacturing (FFF) method, and NinjaFlex is a popular TPU filament for FFF that exhibits an extensive strain range of up to 600%, ideal for the field of soft robotics [45, 46, 47]. Soft robotic applications typically see reduced actuation forces, as the robot's stiffness is significantly lower than in rigid applications. The expected actuation forces range from 0.2N to 20N [23, 48, 3]. As soft robots exhibit large deformation, cable deflection can be high. However, most applications, such as grippers, are made up of several segments in which the cable experiences a deflection below 90^o [12, 3]. Thus, the total deflection may be large, but the deflection over individual friction contacts stays relatively low.

2.1.3 Experimental methodology

Cable friction has been studied for varied applications, each with its own testing approach, and it is important to develop a test rig that is most similar to the desired use case [49]. For example, experimental studies on yarns with driven rollers will use one roller followed by a tensor sensor, a friction surface, a pulley and finally another driven roller to pull the thread [50]. Ghosh *et al.* [51] used a more complicated setup with twisting of the yarn to test the effect of velocity on the fibre friction in the twisting and threading operation. Another testing method involves a sheet of cloth under a sled to falsify the validity of Amonton's law [52]. Podolsky *et al.* [53] investigated the addition of cable guides attached to their robot end effector in hopes of reducing friction and developed a test stand emulating their robot. In summary, previous research demonstrates that a test methodology and stand should resemble the desired application. To my knowledge, no studies have been performed on identifying cable friction over softer material or in the context of soft robotic applications.

2.2 Gripper Design

2.2.1 Soft grippers in food industry

Soft robots have become synonymous with grippers for the food industry. Their ability to grasp fragile objects and conform to a wide range of non-standard geometries present many advantages over their rigid counterparts. Soft robotic grippers come in many different formats. Some notable grasping mechanisms are suction, enveloping, and finger-based soft robots [54]. Without going through an exhaustive list of all available grippers in each category, we will present some examples as well as the benefits and limitations of each approach. Suction-based grippers represent the most compact option as they only require contact with a single surface. However, they are susceptible to air leakage if the contact between the membrane and the surface is not well established [55]. This can be due to non-standard shapes, porous structures or liquids found on the object. There are also commonly combined with other gripping approaches to increase their capabilities, like by combining a finger and a suction cup [56]. However, this increases the weight and complexity of the gripper.

Enveloping grippers cover most of a target's surface, are generally actuated using a single actuator, and can grasp various shapes given certain trade-offs. If objects are spherical, such as tomatoes, apples, eggs, and grapes [54, 57, 58], then the circumferential gripper works very well. However, as shapes deviate, deformation of the gripper around the object is required, meaning the object needs to be stiffer and not get damaged as it indents itself into the gripper. Additionally, as the gripper mostly uses friction to lift objects, weight can be an issue.

One of the most popular grippers in the field of soft robotics are finger-based grippers as they can be cost effective, relatively easy to fabricate and serve as an adaptable component to more complex configurations. Current soft robotic grippers are typically composed of an array of the same finger in different layouts, as developed by Schmalz [59], Soft-Gripper [21], or Rochu [60]. The design approach of these products is on creating a singular soft robotic finger which can replicated and arranged in various generic layouts [61]. Although being able to select from multiple layouts can be seen as positive, it also adds significant overhead. A new layout will change the mass, center of gravity, collision profile, grasping strategy, and require recalibration and validation of the system. A large portion of the finger based grippers have 2 to 4 fingers equally distributed around the centre of a palm, or opposing each other [62]. By utilizing a parallel finger arrangement, this configuration can effectively handle cylindrical items such as bananas, cucumbers, and eggplants [63], while a centred configuration is better for spherical foods like apples, oranges, and kiwis. Finger-based grippers can also be used to grab loose items such as noodles [64]. Many actuation methods can be used, from tendons to pneumatics and even magnets [65] depending on the design objective.

2.2.2 Design of finger-based grippers

The design of soft robots poses unique challenges due to their near-infinite degrees of freedom, non-linear material behaviour of elastomers, and the variety of available manufacturing and actuation methods. This combination creates a highly complex design space. To simplify the problem, soft robotic fingers are often modelled as discrete systems, where the points of deformation are represented as joints [12, 13, 11].

This approach allows researchers to understand and exploit the unique behaviours of compliant structures in a localized manner.

A significant area of research focuses on controlling joint stiffness, which directly influences finger deformation. Some works address this by manipulating the material distribution within joints, effectively developing meta-materials [66]. Others investigate the effects of joint geometry on stiffness and deformation [67]. Another work added functionality to the finger by adding a layer jamming mechanism to dynamically increase joint stiffness to stabilize grasped objects [68]. While these studies provide insights into parameters and mechanisms influencing joint behaviour, they often rely on abstract performance metrics, neglecting the grasp shape. The approaches that prioritize the final shape of the gripper, often derived from force distribution on the object being grasped. For instance, works utilizing conformation and adaptive structures [69] or topology optimization methods given a desired input and output force [70]. However, these strategies don't consider how the gripper deforms to achieve the desired shape.

A parallel strategy is to replicate the behaviour of human fingers, which intuitively adapt to grasping tasks. Salvietti *et al.* [12] demonstrated the potential of joint-based, tendon-actuated soft robotic fingers by optimizing joint stiffnesses to reproduce the trajectory of a hypothetical sixth finger's tip. Expanding on this, my previous work [71] introduced a friction model for elastic cables on elastic surfaces, and modifying the cable routing path within a soft finger to replicate tip and joint trajectories for an arbitrary grasp strategy. Similarly, Connolly *et al.* [72] used a pneumatic soft robot to mimic the deformation path of a human finger. While effective, this work lacked explicit motivation the chosen deformation path. Li *et al.* [73] more recently worked on this limitation by investigating the kinematics and motion patterns of human fingers to understand their underlying grasp strategies.

Beyond individual fingers, most soft robotic hands are developed for prosthetic applications, where priorities include geometry, weight [3], cost [74], and actuation mechanisms [75]. Some works incorporate embedded sensors to determine the current configuration of the hand [76]. Zhou *et al.* [77] extended this concept by controlling actuation based on object sensing, allowing fingers to adaptively deform until contact is achieved. However, this approach focuses on reactive grasping strategies driven by

sensory feedback rather than proactive, structure-driven grasp strategies.

2.3 Simulation of Soft Robots

As the complexity of designs and the need for more accurate simulations increases, simulation solutions will have to adapt and increase their performance for non-traditional actuations and use cases. When modelling the human body, many parts can be treated as non-linear materials for more accurate simulation, such as the extensors and tendons in the human hand [35]. Some soft robots also utilize the non-linear behaviour to enable unique deformations [78], while others require accurate, fast simulation for topology optimization [79]. With the complexity of near-infinite degrees of freedom allowed by soft robots, fast and accurate simulations must be developed to enable non-heuristic control [80].

The traditional analysis methods for physical systems involved using Newton's second law to accumulate forces and solve for accelerations. This translates into velocities and, finally, positions of nodes. This process is time-consuming and requires a deep understanding of all the inputs and phenomena happening in the simulation. This has lead to the pursuit of different discretization methods and simulation frameworks. There have been some voxel-based approaches [26, 81], others try to simplify the calculations by implementing various forms of mass-spring systems [82, 25]. Model reduction techniques which mapped larger, more complex meshes to reduced meshes, increased performance with minimal loss of accuracy [83, 36, 27]. Although these methods improve the traditional approach in terms of speed, many sacrifice accuracy or robustness in terms of material properties in exchange for visual plausibility.

Work has also been done in terms of material research and quantification. Some research has focused on simplifying non-linear material behaviour and developing new models to reduce the computational cost. Some models have been created using principle stretches to generate spline-based material curves [84]. Others have used linear regression of hyperelastic materials to better estimate the Hessian matrix for optimization, which would reduce the number of times the global stiffness matrix would need to be recomputed [24]. Smith *et al.* [85] propose a new method to get a more stable energy term from the Neo-Hookean formulation, which results in more

stable and probable deformations for hyperelastic material. With the advancement in neural networks and deep learning, non-linear material behaviour has also started being modelled and studied to reduce computation time [86].

A simpler approach to FEM coined in 2007, position dynamics, was proposed to deal with nodal positions for simulation directly [87]. This would remove much of the calculations and enable a new way of thinking about interactions, dynamics and simulations. A subdivision of position dynamics is the interpretation of the nodes or elements as geometry constraints that can be mixed and solved. This allowed to quickly characterize a designer or modeller's understanding of deformation without requiring in-depth knowledge on what forces would cause this [88]. This was further extended upon with the notion of as rigid as possible deformation, geometric elements that purely focused on maintaining their initial shape [89]. A survey on position-based dynamics highlighted the use of goal positions instead of internal constraints to match initial shapes to deformed configurations [28]. Shape functions for target deformations were introduced for further applications of the geometry-based approach [90]. The approach also led to new optimization frameworks such as the local-global approach [91] which was fine-tuned by Bouaziz *et al.* [92] and presents new constraints based on geometry. This enabled the simulation of smart materials through a shape matching algorithm [29] and coining of the term Geometry-Driven-Finite-Element. A more interactive and intuitive way of modelling soft robot interactions was developed, showing a performance leap for the state of the art simulation through the help of GDFE [30]. Although these methods provide a new way of defining deformations, they cannot simulate non-linear material behaviours without utilizing traditional FEA methods.

Chapter 3

Modeling Elastic Cable-Surface Friction for Soft Robots

3.1 Introduction

A fundamental challenge in tendon-driven soft robotics lies in accurately modelling friction between cables and deformable surfaces. Additionally, the use of 3D printing as a predominant manufacturing option for soft robots creates new paradigms, surface interactions and material combinations that have yet to be explored. Cable friction is influenced by surface compliance, contact asperity, and deformation. This motivates the central question of this chapter: *How to integrate the inherent asperity and elasticity of the contact surface in cable-actuated soft robots into the modelling of friction behaviour?* Building upon the observation that a decrease in cable tension corresponds with an increase in surface area and thus its adhesion effect, the objective is to test the hypothesis that the asperity behaviour of an elastic contact surface with an elastic cable demonstrates a negative linear relationship with the holding tension.

To test this hypothesis, four different material interactions, consisting of two cables and two surfaces, are evaluated. The selected cables include a generic twine and a braided fishing line, while the friction surfaces are made of Polylactic Acid (PLA) plastic and thermoplastic polyurethane (TPU), common 3D printing materials used in soft robotic applications. A unique test setup and process are developed to measure a cable's incoming and outgoing tension passing over an elastic frictional surface. Multiple tests are performed at varying angles of cable deflection and loading cases. The results are analyzed using established models, and my novel formulation is presented

in this chapter. To validate the new model, the fingertip trajectory of a 3D-printed soft gripper is tracked and compared to a kinematics formulation. Finally, I designed a soft robotic finger which emulates our intuition of uniform deformation by utilizing my new model and optimizing the routing path of the cable within the finger. The contributions of this work are summarized as follows:

1. I propose a novel friction formulation to account for the asperity behaviour of the friction surface and accurately model how an elastic cable slides over an elastic surface.

2. I develop a new method and test setup to efficiently determine the friction coefficient for soft robotic applications with a few data points to reduce the number of physical tests needed.

3. The design of a soft robot given a grasp strategy is demonstrated through the optimization of the routing path of the cable actuation.

The chapter is structured as follows: Section 3.2, I describe my testing methodology, test stand, kinematic model, and introduce the different cable friction models. The experimental test results and the performance of varying friction models, including the Capstan model, Heap *et al.*'s model, and my new formulation are presented in Section 3.3. Section 3.4 presents the design of a soft robotic finger given a grasp strategy. Finally, Section 3.5 presents this chapter's conclusion.

3.2 Methodology

3.2.1 Materials and Experimental Setup

Previous research shows that friction between a cable and a cylindrical surface depends on many factors. These factors include the cable and cylinder material, the applied load, the cylinder's radius, and the testing procedure's speed. In this work, the variables investigated are the contact surface materials made of PLA (generic) and a TPU (NinjaFlex), as well as two different cables: $1.5mm\varnothing$ polypropylene (PP) twine and a $0.25mm\varnothing$ polyethylene (PE) braided fishing line. The other parameters are constants based on commonly used parameters in soft robotic applications: the

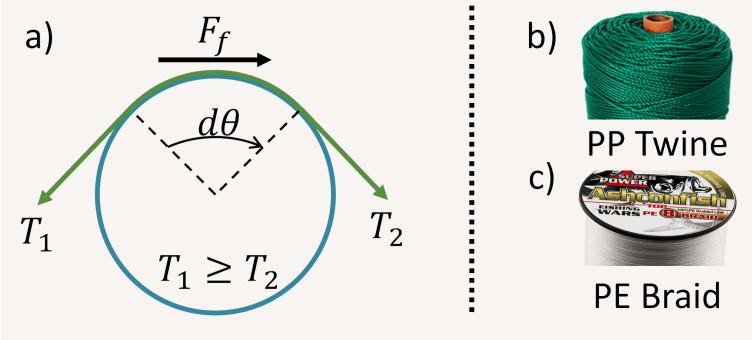

FIGURE 3.1: a) Friction convention for a cable sliding over a cylindrical surface. b) Polypropylene twine. c) Polyethylene braided fishing line.

radius of the contact surface of $3mm$ and a cable actuation speed of $40mm/min$. Figure 3.1 displays the cables and conventions used for this chapter. The incoming and outgoing tensions of the cable are T_1 and T_2, respectively. Angle $d\theta$ is defined as the change in the angle of the cable over the friction surface. For simplicity, the holding force will always be T_2, while the pulling force and the direction of slip will always be toward T_1.

The test stand is a modification of the ASTM D3108 standard [42] for determining the friction coefficient between yarn and solid material and can be seen in Fig. 3.2. As the wrap angle is significantly less, changes constantly during use, and the contact surface is not a perfect cylinder, four modifications are made to the ASTM D3108 test stand. The first change is to use a linear stage to pull the cable to ensure constant speed instead of a winding spool. The second is that instead of moving only the friction surface to change angles, a guide pulley can also easily be raised or lowered. Third, the friction surface is modular and can easily be replaced with different geometries or materials based on the use case. Lastly, the load is established by a known hanging weight instead of a tensioning pulley. These changes create a compact, modular, and flexible test setup that can easily adjust for different contact angles, loads, materials, and geometries. T_1 is determined by a load cell connected to the linear stage, in this case, an ESM750 tensile test machine. The cable under investigation is connected to the load cell and passes over the pulley and then over a rounded 3D printed surface of PLA or TPU, detail A in Fig. 3.2. The print orientation of the contact surface mimics the optimal print orientation of the grippers used for validation in Section 3.3. As such, parts are printed on their sides such that the layer lines run parallel to the direction of

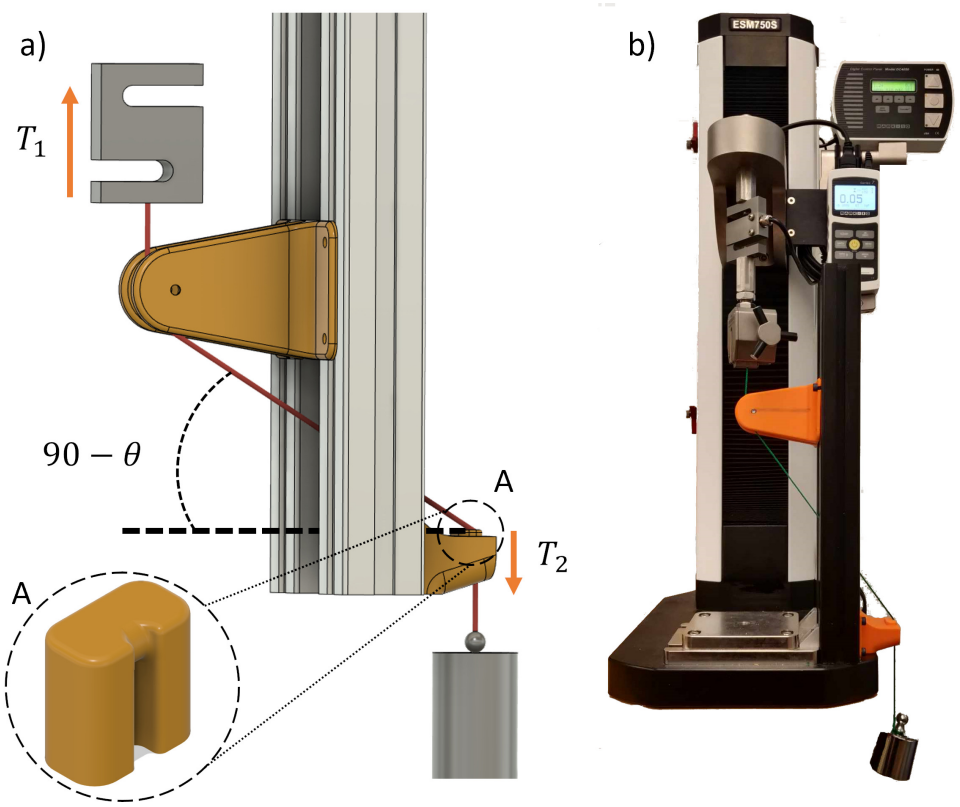

FIGURE 3.2: Cable friction test stand: a) CAD model, and b) Physical setup. The linear stage raises the load cell, pulling the cable over a pulley and friction surface in detail A. T_2 is set by attaching known weights to the other end of the cable.

the cable with a layer height of $0.2mm$. The end of the cable is subsequently attached to known weights, which dictate the tension T_2. By comparing T_1 to T_2, it is possible to obtain the effect of friction on the selected material combination at different angles and loading scenarios. A total of 45 test cases were performed. Theta is incremented from 10^o to 90^o in increments of 10^o, and incrementing T_2 in steps of $200g$ from $200g$ to $1kg$. Note that this test stand is entirely modular and can be adapted to multiple materials and contact surface geometries.

3.2.2 Kinematic Formulation

The mathematical formulation for the kinematics of a two-dimensional soft finger can be expressed as the system of forces acting on the finger [12]. It is possible to relate the cable displacement d directly to the joint configuration q as $d = d(q)$. This relationship can be further linearised for small deformations: $\delta d = D(q)\delta(q)$, where $D(q)$ is the Jacobian of $d(q)$. For this study, it is assumed that there are no other

contacts with the finger, both acceleration and velocity are relatively low, and the effect of gravity is negligible compared to the finger stiffness. As such, the Jacobian becomes a transformation matrix [93], and we can describe the forces F acting on the finger as vector τ_a:

$$\tau_a = D^T F \tag{3.1}$$

The resistive forces $\tau_p(\Delta q)$ with respect to the rest position q_0 can be expressed as a function of their current configuration, i.e. $\Delta q = q_0 - q$. By combining the forces acting on the system and the resistive forces, the system can be expressed as:

$$\tau_a + \tau_p(\Delta q) = 0 \tag{3.2}$$

Similarly, by only considering small variations, this relationship can be linearized:

$$\delta\tau_p = -K_q \delta q \tag{3.3}$$

Therefore, the system can be approximated as $\tau_a = K_q(q)\delta q$. The relation introduces a symmetric and positive definite joint stiffness matrix K_q. In the general case, K_q depends on the geometry, material properties, and configuration of the joint. For a given design, K_q is constant. More specifically, the stiffness of an individual joint is assumed to be a torsion spring and expressed as:

$$K_{q,j} = \frac{EI}{l \times r_j} \tag{3.4}$$

Where E is the Young modulus of the material, I is the moment of inertia, and l is the length of the joint. The Young's modulus of the TPU is $21.89MPa$ based on my print settings of 100% infill using a line infill pattern [94]. The distance from the center of the joint to the contact point is represented by r_j and is included directly in K_q to convert the moment generated into a force.

Friction Consideration

The effect of cable friction is commonly expressed as a ratio between the tensions of a cable deflecting over a surface, i.e. $R_f = T_i/T_{i+1}$. In this chapter, R_f is defined by either the Capstan model, Heap *et al.*'s model, or my model. Each model is further

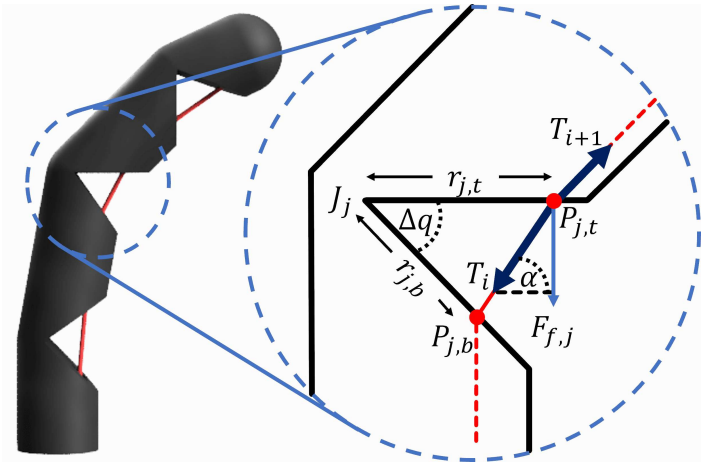

FIGURE 3.3: Free-body diagram of joint model.

described in section 3.2.3. To ensure the actuation force is equal to the resultant forces of the system, we can first calculate the tension at the tip as $T_n = T_a/R_f$, where n is the number of routing or contact points the cable must pass over. It is noted that R_f can be used to compare any two points on a cable regardless of the number of contact points it passes over, as long as the total deflection between them is considered. Working backwards from there, we can calculate the friction forces acting on each routing point as $F_{f,i} = T_i - T_{i+1}$. To achieve equilibrium, the actuator tension must be equal to the tension in the finger, resulting in equation 3.5 below:

$$T_a = \sum_{i=1}^{n-1} F_{f,i} + T_n \tag{3.5}$$

From this equation, we can populate the force vector τ_a applied to the system of joints from Eq.3.2, where $\tau_{a,0} = T_a$ is the force from the actuator, $\tau_{a,m} = T_n$ is the resultant force at the tip of the finger and m is the number of joints. The friction force at a contact point that contributes to the bending of the joint is calculated by first taking the angle α_j between the tension vector $\overrightarrow{P_{j,t}P_{j,b}}$ and the vector connecting the joint and the contact point $\overrightarrow{J_jP_{j,t}}$, depicted in Fig.3.3. The force contribution to joint deformation is $\tau_{a,j} = F_{f,j} \cdot sin(\alpha_j)$. It is noted that R_f is dependent on the configuration of the system; as such, the model is path dependent and must be solved by incrementally increasing or decreasing the actuation force. The resulting equation to calculate the force contribution to joint deformation is:

$$\tau_{a,j} = T_{2(j+1)-1}(R_f - 1)sin(\alpha_j) \tag{3.6}$$

This equation considers all losses in tension between $P_{j,t}$ and $P_{j+1,t}$ as contributing to the deformation of joint j. Thus, R_f should also be calculated as the tension ratio between $P_{j,t}$ and $P_{j+1,t}$.

Cable Contact

To determine if friction occurs, contact detection between the cable and the passage is done by calculating the distance of the current routing point to a line formed by the previous and next routing point. As the passage is cylindrical, once cut to make room for the groove, an elliptical shape remains, where the minor axis is the same as the initial radius, and the major axis is extended. If the distance is less than the major axis length minus the cable radius, then there is no contact between the cable and the body, and thus there is no friction.

3.2.3 Friction Models

Capstan Model

The Capstan model is one of the oldest cable friction models, dating back to the 1780s, and is still the most popular model because of its elegance. The ASTM D3108 standard currently recommends it and is stated to be sufficient to determine the friction interaction between a cable and a friction surface [42]. The formulation transforms Amonton's law of friction, which correlates normal force to friction force, into a multiplicative relationship between holding and pulling tension. By discretizing a cylindrical surface into infinitely small linear segments using the small angle approximation, the capstan model simplifies the relation between the two tensions as being factors of the total deflection angle, θ in radians, of the cable over the contact surface multiplied by a friction coefficient μ raised to the exponential, as depicted in Eq. 3.7 below. This model assumes that the friction coefficient between two surfaces is constant and that the friction factor R_f is solely a function of the deflection angle.

$$R_{f,capstan} = e^{\mu\theta} \tag{3.7}$$

Heap *et al.* Model

Research published since the 1950s [39] has demonstrated that the material characteristics of the cable also affect the friction factor. The formulation refined by Heap *et al.* builds upon the observation that cable rigidity will also affect R_f. This observation takes into account two factors. The first is the total bending radius $r = r_c + r_s$ of the cable, which describes the contact surface area with the deflection angle, where r_c is the cable radius and r_s is the surface radius. The second is the effect of the holding tension on the friction factor. The increase in load compresses the small contacts into larger areas, decreasing the effect of friction as is consistent with elastic deformation [95]. This model proposes an effective friction coefficient μ_e, which decreases as the load increases. This formulation now requires two coefficients to fit the data, α and n, and includes T_2 as an independent variable alongside θ.

$$
\begin{aligned}
R_{f,Heap} &= e^{\mu_e \theta} \\
\mu_e &= \alpha \left(\frac{r}{T_2}\right)^{1-n} \left(\frac{\ln(1+K)}{K}\right) \\
K &= -\alpha(1-n)\left(\frac{r}{T_2}\right)^{1-n}\theta
\end{aligned}
\tag{3.8}
$$

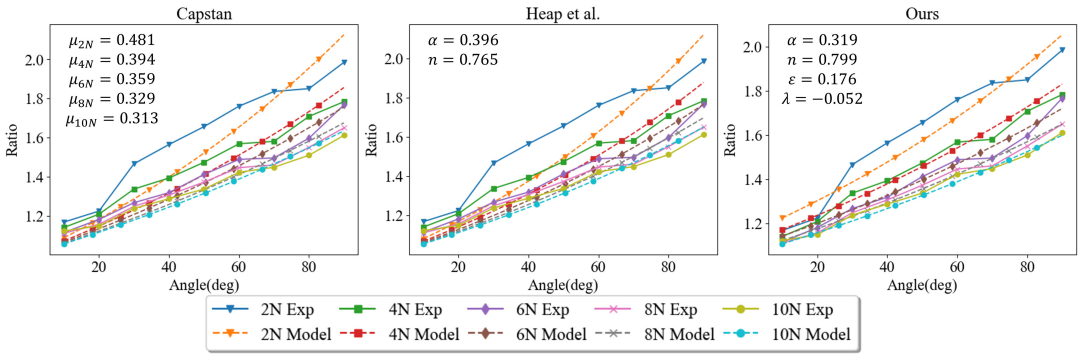

FIGURE 3.4: Comparison of the friction models to the Twine & TPU data. Left: Capstan Model with a unique μ for every load, Middle: Heap *et al.*, Right: my model.

My Model

Previous models have considered the behaviour of the cable in relation to the friction factor. However, the role of the contact surface has not been explored. In soft robotics, we no longer deal with a rigid polished surface, as in previously developed models. We

must consider how an elastic and relatively rough surface affects friction. Combining a fibrous surface with a 3D-printed surface creates a higher asperity contact. Therefore, it is theorised that a baseline adhesion force exists, described as a hook-and-loop interaction. Meaning that friction still exists even if the normal force is zero, *i.e.*, $\theta = 0$. It is noted from previous models that an increase in tension reduces the asperity of the cable due to deformation and thus reduces the effective friction coefficient. Based on the assumption that the asperity of the contact surface follows a similar negative logarithmic behaviour a new term is added to Heap *et al.'s* model. The coefficient ϵ represents the initial friction effect, and the decrease of this force is captured by $\lambda \ln(T_2)$. The proposed formulation is described below in Eq. 3.9.

$$R_{f,Ours}(\theta, T_2) = e^{\mu_e \theta + \epsilon - \lambda \ln(T_2)} \tag{3.9}$$

where μ_e has the same formulation as Eq.3.8 composed of coefficients α and n, and θ is the deflection angle of the cable.

3.3 Results

In this section, I present the results of the experimental tests. I initially investigated the combination of a twine cable and a TPU friction surface. I fit the data using the Capstan friction model, Heap *et al.'s* friction model and my new formulation. The fitting performance alongside the tip position estimation using the kinematics model in Sec. 3.2.2 is presented for the three friction models. Three additional material combinations are also tested to validate the formulation: twine & and PLA, Braid & PLA, and Braid & TPU.

3.3.1 Twine & TPU Fitting

Figure 3.4 shows the twine and TPU combination test data for all three mathematical models. The x-axis denotes the deflection angle, and the y-axis represents the tension ratio R_f. The different plots correspond to the various loading conditions. From the experimental data, it is clear that two factors affect the ratio between the input and output tension. The first is that an increase in deflection angle increases the tension ratio, as noted by most cable friction formulations, and the second is the effect of the

load T_2. As T_2 increases, it is seen that the tension ratio decreases. It should also be observed that as $\lim_{\theta \to 0} R_f(\theta, T_2) \neq 1$, meaning there still exists some form of friction despite no normal force.

Fitting the data using only the Capstan equation is ill-advised as a single value for μ only considers the effects of the deflection angle and not the properties of the materials interacting. A unique value of μ is calculated for every load T_2 to obtain a valid fitting. The results of the multiple fittings can be seen in Fig. 3.4. Even with accounting for several friction coefficients, the average error is 4.1%, and a max error of 12.3%. Heap *et al.'s* model addresses one of the limitations of the Capstan model by including the effects of T_2 on the cable in the formulation. Additionally, its coefficients, α and n, can be fitted to all test cases simultaneously to obtain one equation for the combination of materials. In the case of twine and TPU, the coefficients are $\alpha = 0.427$ and $n = 0.731$. The results of this fit can be seen in Fig. 3.4. Although this is a more general approach that accounts for both deflection and loading, it still has the property of the Capstan model, where the formulation converges aggressively to a R_f of 1 with smaller deflection angles. The average error of Heap *et al.'s* formulation is 4.12% with a maximum error of 12.33%. The fitting error is very similar to the capstan model, demonstrating that the formulation extends the capstan model for multiple load cases and achieves an R^2 value of 0.902.

Our model was fitted to the data obtained from the twine and TPU experiments, demonstrating a strong fit. The coefficients for the model are $\alpha = 0.319$, $n = 0.799$, $\epsilon = 0.176$ and $\lambda = -0.052$. The average error is 2.2%, with a max error of 6.26% and a R^2 value of 0.966. The model is nearly twice as accurate as the previous models. The increase in accuracy can be attributed to the ability to capture the friction when θ is small, allowing my model to shift along the y-axis. This results in a relatively flatter curve than the other two models, and thus does not overcompensate for higher values of θ.

3.3.2 Other Material Combinations

To validate the generality of my model, I explore three additional contact types. Namely, twine & PLA, braid & PLA, and braid & TPU. The braided cable is significantly thinner than the twine cable and less extensible. PLA is significantly stiffer

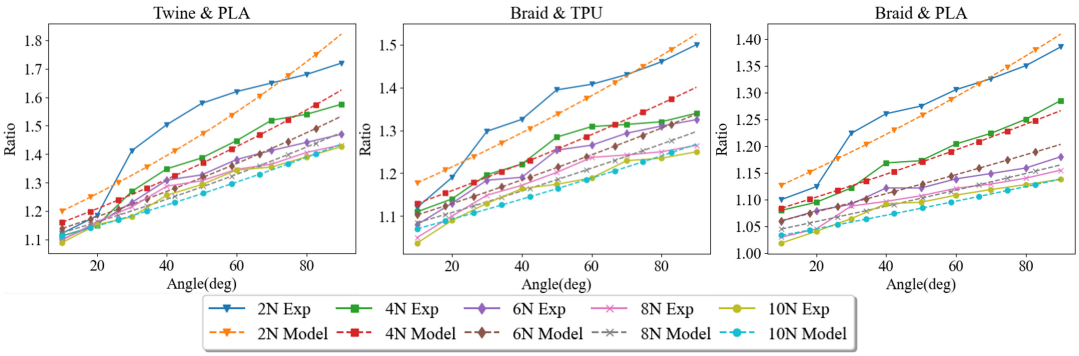

FIGURE 3.5: Fitting of my model to the data for Left: Twine & PLA, Middle: Braid & TPU and Right: Braid & PLA.

TABLE 3.1: Fitting performance of the Capstan, Heap et al.'s, and my model using 45 data points for each material configuration.

	Average Error			**Max Error**			**R^2**		
Model	Capstan	Heap	**Mine**	Capstan	Heap	**Mine**	Capstan	Heap	**Mine**
Twine & TPU	4.10%	4.12%	2.20%	12.26%	12.32%	6.26%	0.902	0.902	0.966
Twine & PLA	4.59%	4.60%	2.55%	12.56%	12.59%	7.73%	0.754	0.751	0.925
Braid & TPU	3.69%	3.72%	1.67%	9.95%	10.00%	5.09%	0.637	0.628	0.914
Braid & PLA	2.13%	2.19%	1.07%	7.55%	7.42%	3.32%	0.726	0.704	0.925

than TPU; however, it is still ductile and elastic when compared to metals that are traditionally investigated. Additionally, it will also have similar 3D-printed surface roughness. The three new combinations are tested using the same procedure outlined in Sec. 3.2. The resulting fit can be seen in Fig. 3.5, and the errors of all three friction models are reported in Table 3.1. The constants for the different fittings of my model are listed in Table 3.2. The four combinations of materials have an average error of less than 1.9% and a maximum error of less than 7.7% using the new model. The Capstan model has already been shown to be inadequate as it does not account for cable loading. Heap *et al.'s* model has an average error of 3.7% and a maximum error of 12.6%. Although its average error is low, the average R^2 is worse at 0.746 compared to the new model's value of 0.932.

TABLE 3.2: Constants for my model

Materials	α	**n**	ϵ	λ
Twine & TPU	0.3195	0.7990	0.1761	−0.0521
Twine & PLA	0.2456	0.7104	0.1575	−0.0356
Braid & TPU	0.1595	0.7446	0.1673	−0.0525
Braid & PLA	0.1211	0.5047	0.1236	−0.0450

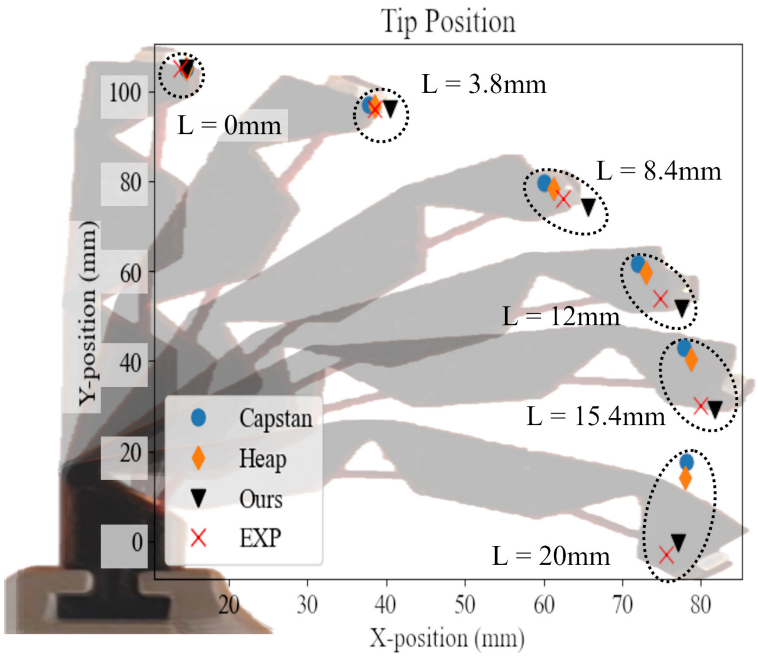

FIGURE 3.6: Tip position of soft robotic finger at different cable actuation lengths comparing the accuracy of the Capstan model, Heap *et al.*'s model, and my model.

3.3.3 Tip Trajectory Matching

The example presented in Fig. 1.2 in the introduction shows a gripper with uniform joint geometries, uniform material properties, and a cable routing path, which ensures that all joints have the same r_j. This was selected as a test case to test the intuition of uniform deformation and isolate for the effect of friction. Using the kinematic model from Sec. 3.2.2 and the different friction models for R_f in Eq.3.6, we can see that at $20mm$ of actuation, only my model (Fig. 1.2d), resembles the experimental case (Fig. 1.2e). To further illustrate the accuracy of the models, I compared the trajectory of the fingertip throughout the actuation. A single finger from the gripper is reprinted, and the location of each joint and fingertip is tracked using markers and recorded using a video camera. The image data is then processed to calculate the position of the joints, tip, and joint angles throughout the deformation. The theoretical behaviour of

the different friction models is simulated using the mathematical formulation outlined in Sec. 3.2.2, and the resulting tip position is plotted alongside the experimental values in Fig. 3.6 at different actuation lengths L. The resulting tip position error for the Capstan model is 9.74%; for Heap *et al.*, it is 8.05% and 1.23% for my model.

At the start of the actuation, all three models performed similarly. As a joint deforms, the cable deflection increases, thus R_f increases. Therefore, any additional force from the actuator is decreased by $T_n = T_a/R_f$. The critical observation is that, in the experimental case, the joint closest to the point of actuation deforms significantly more than the other joints. Therefore, R_f must be significant at the beginning of the actuation. From Fig. 3.4, we can see that both the Capstan model and Heap *et al.*'s model have a much higher R_f when θ is large, compared to my model. However, friction is path-dependent; its effects get compounded the more the finger is deformed. An equilibrium is reached for every increment of ΔT_a, not for the total force in the system. If friction is underestimated, this compounding effect lags, and a more uniform deformation occurs. This experiment highlights the impact of the friction factor when $\theta = 0$, which is captured by my new formulation. It should also be noted that although Heap *et al.'s* model has a relatively low average fitting error of 4.1%, the large initial error, maximum error, and the path dependency of soft robotic applications make it unsuitable.

3.3.4 Minimum Tests Required

As there is currently no predictive model for the friction interaction between two elastic materials, experiments such as the one presented in this chapter are necessary to fit any mathematical model. Therefore, limiting the number of experiments to obtain a reliable fitting is important. The fitting process was performed on the four test cases using only 9 data points instead of the original 45 to demonstrate the lower limit of the required tests. As the model has several logarithmic terms and an exponential aspect, having data points that represent the future use case is important. Extreme extrapolation of either of the design variables, be it weight or angle, could lead to asymptotes in the fitting where either there is a cross over one of the axes or infinite values for R_f. The recommended points are the minimum and maximum expected loads and an additional data point splitting the range. Similar logic is used

TABLE 3.3: Error of my model using 9 points, difference from 45 data points in brackets.

Materials	Average Error	Max Error	R^2
Twine & TPU	2.20% (−0.04)	6.26% (+0.64)	0.966 (+0.001)
Twine & PLA	2.54% (+0.39)	7.74% (+1.88)	0.925 (−0.033)
Braid & TPU	1.66% (+0.2)	5.08% (+0.06)	0.913 (−0.026)
Braid & PLA	1.07% (+0.21)	3.31% (+1.02)	0.925 (−0.030)

for the selection of angles. The weights selected are $200g$, $600g$ and $1000g$, and the angles used are 10^o, 50^o and 90^o. Table 3.3 details the results of the fitting. The results show that using 9 data points accurately depicts the friction interaction for all four material combinations. Additionally, performing the same validation with the soft gripper gave an error of 1.12% compared to 1.23% for the 45 data point case. This results in a difference of $0.115mm$ within the measurement error margin. Thus, drastically lowering the required data points did not change the new model's accuracy over the entire range of experimental values.

3.4 Design of Soft Finger

Using the formulation presented in this chapter, a soft gripper that follows a tip path or a grasping strategy can be designed. For this work, a grasping strategy refers to the order in which the joints deform and dictates the initial contact points with objects and the force distribution. Looking at the example from Sec. 3.3.3 reproduced in Fig. 3.7a, where the cable was equidistant to each joint, meaning $r_i = 8.5mm$ for all routing points, the first joint deforms the most, then the second and finally the third. This order of joint deformation would be preferred in power grasp applications, but undesired for precision pinching applications. This section aims to demonstrate that carefully placing cable routing points makes it possible to change the grasping strategy arbitrarily. The selection of the routing points will dictate both the effect of friction and the moment applied to each joint. Specifically, the objective is to select the distance of the routing points to have all joints deform uniformly throughout the actuation of $20mm$. The routing points are defined as the entrance and exit for each joint. The location of the entrance and exit points are dictated by their distance from their joint along the opening, as can be seen in Fig. 3.7a. In this example, the finger

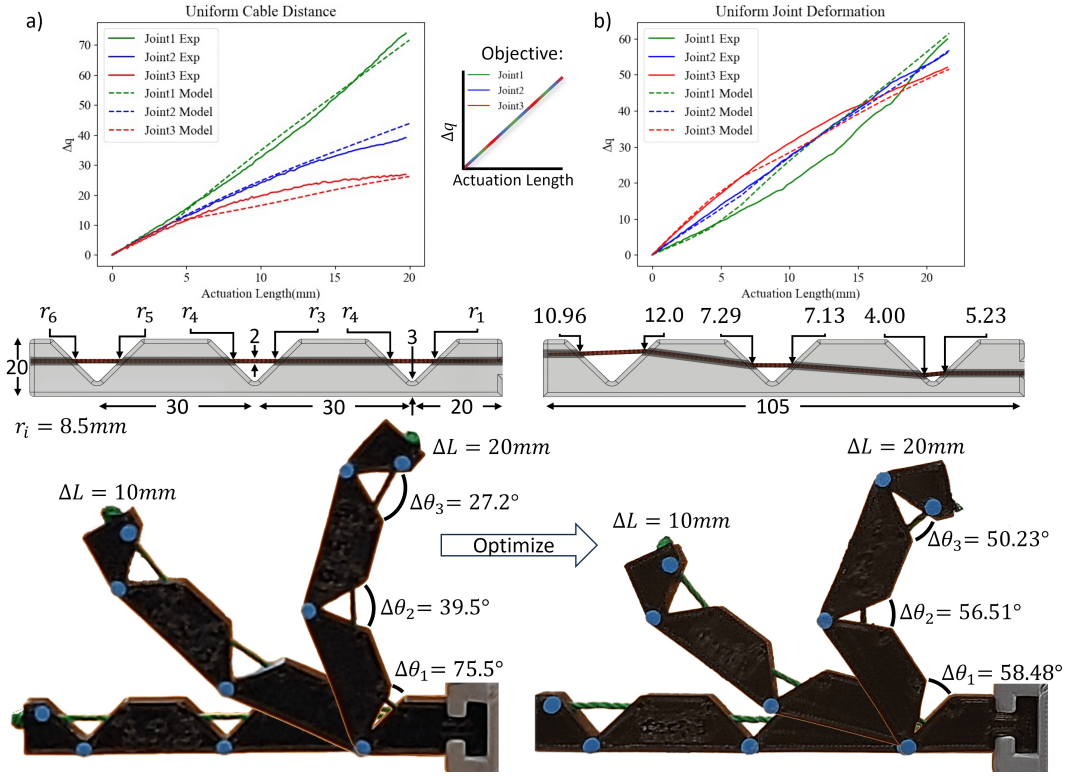

FIGURE 3.7: a) Finger with uniform routing path where $r_1 = r_2 = r_3 = r_4 = r_5 = r_6 = 8.5mm$. b) Finger with cable routing path optimized to obtain uniform joint deformation throughout actuation. Top: Comparison of the joint deformation vs. actuation length. Middle: CAD model with respective positions of cable routing distances r_i. Bottom: Snapshots of video recording during actuation. All measurements are in millimetres.

has three joints, and thus six independent variables to be optimised. The distance between joints is set as a constant $35mm$; all joints have the same stiffness and have a 90 deg opening. The finger's width is $13mm$, and the thickness of the joint is $3mm$.

The kinematic model from Sec. 3.2.2 is implemented in Python and the SciPy.optimize library is used for the optimisation. The Sequential Least Squares Programming (SLSQP) method is the minimisation algorithm, with bounds set from $4mm \rightarrow 12mm$ for each routing point. The error is obtained by calculating the average deformation of the three joints $q_{avg,i}$ in each iteration i as the cable is slowly pulled over n iterations until the actuation length reaches $20mm$. The difference $q_{j,i} - q_{avg,i}$ for all three joints are summed, and the root-mean-square error (RMSE) is calculated from those values as outlined in the equation below:

$$RMSE = \sqrt{\frac{1}{n}\sum_{i=0}^{n}\sum_{j=0}^{3}|q_{j,i} - q_{avg,i}|} \tag{3.10}$$

After optimization, the routing point distances obtained from the closest to the actuator to the farthest are $5.23mm, 4.00mm, 7.13mm, 7.29mm, 12.00mm$, and $10.96mm$, resulting in an RMSE of 4.7 for the objective of all joints deforming equally throughout the deformation. The design is 3D printed, and its deformation is compared to the theoretical model in Fig. 3.7b. The RMSE of the theoretical model and experimental is 6.1. As multiple non-linear effects occur simultaneously, it is interesting to note the strategy used to attempt this objective. As joints deform, the contact angle for the cable will significantly increase the effect of friction. As such, the joints furthest from the actuator must have the largest moment arm. However, since friction has an exponential correlation with deformation, there is a crossover point where the joints closer to the actuator start rapidly deforming, and those further away begin to slow down. In particular, the crossover point occurs at $12.3mm$ of the actuation in this example. Interestingly, the optimised result has $r_2 < r_1$, resulting in a smaller moment arm, leading to slower deformation at the start. However, it increases the cable deflection at r_2, leading to a more significant frictional effect. As such, the optimizer is aware that it is impossible to have completely uniform joint deformation in the presence of friction throughout a large deformation with a single actuator and is actively controlling the crossover point to minimize the error. The intuition that all joints should deform equally has not only been proven wrong due to friction but has also been shown to require a significant change in the routing path to counter its effect.

3.5 Conclusion

Developing a predictive model for cable friction poses significant challenges. Previous research has proposed mathematical models for elastic-rigid contacts prevalent in the textile industry. However, an understanding of elastic-elastic contacts, essential for soft robotics, is currently lacking. This work introduces a novel methodology to evaluate friction between an elastic cable and a 3D printed soft material, mimicking

standard contacts in soft robots. Given the complexity of factors, such as 3D printing parameters, surface finish, and cable and surface material properties, establishing a predictive friction model requires experimental tests. Thus, the presented methodology is simple and fast. While the friction model, requires only 9 data points for high accuracy.

The pairing of twine and braided cable to PLA and TPU demonstrated a unique behaviour that current friction models could not characterise. The experiments show that the Capstan model is inadequate for modelling friction in soft robotics applications, as it cannot capture the tension dependency. Similarly, the state-of-the-art model could not capture the asperity effects of low loads and cable deflection. My novel mathematical model considers the contact surface's asperity behaviour, increasing the fit accuracy at small θ and tension values. This new model demonstrated a reliable fit with an average R^2 value of 0.932 in all cases compared to an average value of 0.746 for Heap *et al.'s* model, directly translating into a more accurate simulation of a soft robotic gripper. My model showed a 1.23% error for tip position prediction compared to a 8.05% error for Heap *et al.'s* model. Deformation in soft robots is gradual and is informed by their current state; any error in the estimation of the current state will be compounded into the estimation of the following state. With the mathematical model presented, it was also shown that the design of a soft robot given a grasping strategy is possible by simply modifying the routing path.

Chapter 4

Grasp Strategy-Driven Soft Robotic Grippers for Food Industry Applications

4.1 Introduction

The objective of the work presented in this chapter is to apply group technology to develop a grasp-based product mix, where products are grouped based on their grasp type. By designing grippers which mimic the human hand, tailored to each product mix, I aim to minimize the need for frequent gripper reconfiguration or reprogramming. Within a given grasp-based mix, product variations–such as differences in size or texture–do not necessitate gripper redesigns, enabling a modular approach where a single optimized gripper can handle multiple items efficiently. A major advantage of this approach is that it enables a simplified actuation strategy, eliminating the need to control each joint independently to achieve different grasp types. Instead, the gripper's passive compliance and structural adaptability allow it to conform to various objects within its assigned grasp category. This simplification not only reduces control complexity but also enhances reliability, cost-effectiveness, and scalability in industrial applications, making frequent product changeovers more feasible. In this chapter, I present a design pipeline for developing a tendon-driven, 3D-printed, modular, hand-mimic soft gripper tailored for the food industry. This pipeline is designed to reduce development time and costs while ensuring adaptability and effectiveness in handling a diverse range of food items. For testing, a diverse set of food items

with distinct geometries, sizes, weights, and surface characteristics were selected. The design process starts by observing human grasping actions, and capturing natural interaction patterns with these objects. They are then analyzed to identify and classify grasp strategies, which serve as the basis for grouping food products according to their handling requirements. After that, the joint deformation data is leveraged to optimize the cable routing path and joint stiffness of the tendon-driven soft robotic fingers. The goal is to ensure the fingers follow the natural grasp trajectory observed in human demonstrations while minimizing actuation force. A kinematic model, adapted from previous work [71], is further refined to account for the behaviour of hyperelastic materials, enabling accurate prediction of the soft robotic finger's motion. The optimization process was applied to each finger across the identified grasp strategies. Following optimization, the fingers were individually 3D-printed and validated to ensure they accurately followed the target trajectories. Once validated, the fingers were mounted onto a modular palm structure, assembling a complete gripper. The fully assembled hand was then tested on the same set of food items to verify its versatility and grasping performance. The key contributions of this chapter are as follows:

1. A grasp-based product mix concept that categorizes food products according to their required grasp type. This classification approach enhances robotic adaptability in food automation by minimizing the need for frequent gripper reconfiguration.

2. A streamlined design pipeline that integrate human demonstration data, grasp strategy optimization, and kinematic modeling. This pipeline significantly reduces development time and cost while ensuring effective and adaptable food handling.

3. An optimization framework that improves gripper performance by incorporating hyperelastic material properties, optimized cable routing paths, and joint stiffness tuning. These enhancements minimize actuation force and improve grasp stability and efficiency.

The experimental results demonstrate that the optimization process effectively replicates the intended grasp types and their corresponding motion paths. Additionally,

the 3D-printed grippers successfully grasp and manipulate the selected food items, confirming their functionality and adaptability.

The chapter is structured as follows: Section 4.2, describes how I obtained the grasping path, introduces the kinemtatic model, optimization scheme and modular hand. The validation of the optimized fingers, and soft robotic hand are presented in Section 4.3. Section 4.4 discusses the performance of the each grasp on the totality of the item set and potential improvements to the design. Finally, Section 4.5 presents the chapter's conclusion and suggests areas for future research.

4.2 Methodology

4.2.1 Grasp-based Product Mix

To create the grasp-based product mix, we start by observing a user grasping a carefully selected set of food items, chosen to encompass a wide range of physical properties. The selection includes small, delicate items such as grapes and eggs, alongside larger, more robust objects like oranges and apples. Deformable foods, like bananas and sausages, contrast with rigid and brittle items, such as cracker sheets and frozen pizza, each requiring varying levels of grip force and control. Textural diversity is also represented, ranging from the smooth surface of cheese slices to the rough, uneven exterior of a muffin. Some items, like vine tomatoes or clusters of grapes, introduce irregular, multi-part structures that require intricate finger coordination, while others, such as a bag of chips, present challenges due to their flexible, air-filled packaging. This selection reflects the complexity of real-world grasping tasks by incorporating a broad spectrum of shapes, textures, and structural properties, ensuring a comprehensive dataset that covers diverse handling requirements. Specifically, the objects used in this study vary in shape (e.g., spheres, cylinders, string-like forms, and rectangles), weight (ranging from 5g to 600g), texture (smooth, dimpled, or rugged), and size (with final grasp openings spanning from 1cm to 10cm). This wide variety captures the intricacies of food handling and the corresponding adjustments needed for effective robotic grasping.

Each grasp is analyzed by tracking the movement of individual finger joints throughout the motion. The sequence of joint flexion, the extent of their movement, and the

coordination between fingers provide valuable insights into the type of grasp being employed. By examining these joint movement patterns, we can identify the grasp strategy used for each object. From observing the user grasping the 15 selected objects, three primary grasping approaches were identified. The first and most common involved a relatively uniform deformation across all joints, which corresponds to the **power grasp**. This grasp is characterized by near-simultaneous flexion of all finger joints, forming a strong enclosure around the object for secure handling. The second approach focused on the deformation of primarily the proximal joint, corresponding to the **pinch grasp**. This grasp typically involves early activation of the thumb and index finger, though other fingers may also contribute with similar motion, making it ideal for handling small or delicate items. The third approach involved significant deformation of the middle and distal joints, with minimal movement in the proximal joint, corresponding to the **hook grasp**. This grasp is particularly suited for handling objects with handles or those requiring a more controlled, less enclosing grip. The objects are categorized by grasp type and presented in Table 4.1.

TABLE 4.1: Objects and their grasp types.

Mix	**Objects**
Power	egg, orange, muffin, apple, sausage, banana, baloney
Pinch	grape, cheese slice, cheese cake, cracker sheet, frozen pizza, bag of chips
Hook	tomato vine, grape vine

4.2.2 Gripper Design and Modelling

To streamline the gripper design process, the gripper is structured to closely replicate the human hand's form and function. First, the gripper's dimensions and topology are derived from human hand anatomy, using joint locations and bone segment lengths to guide its structure (Fig. 4.1). This biomimetic approach ensures that the gripper maintains natural articulation and movement patterns, optimizing its adaptability for various grasping tasks. To facilitate modularity and easy interchangeability, the fingers are attached to the palm using mortise-and-tenon joints. This design choice ensures that individual fingers can be replaced without altering the overall geometry, actuation mechanism, or weight distribution of the gripper. The thumb design is inspired by Zhou et al. [96] but has been adapted to fit seamlessly within the gripper's palm

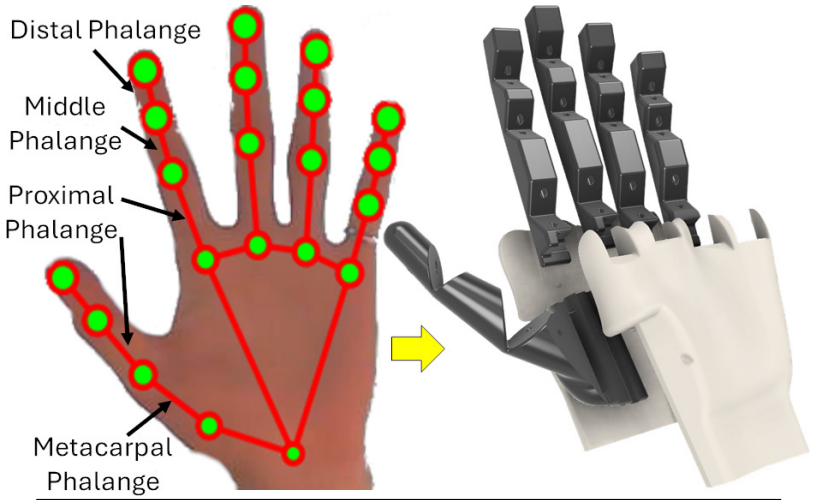

Finger	Metacarpal	Proximal	Middle	Distal
Thumb	60 mm	40 mm	30 mm	-
Index	-	45 mm	27 mm	23 mm
Middle	-	50 mm	30 mm	25 mm
Ring	-	47 mm	28 mm	24 mm
Little	-	38 mm	20 mm	20 mm

FIGURE 4.1: Parametric 3D hand model developed based on human hand anatomy.

structure while maintaining ergonomic efficiency. All fingers maintain a consistent width of 15 mm, except for the little finger, which is slightly narrower at 12 mm to better match human proportions. The gripper is 3D-printed using fused filament fabrication (FFF). The fingers are made from flexible TPU for soft grasping, while the palm is printed from rigid PLA for stability.

Second, to design a gripper that closely mimics human grasping, we model its deformation based on natural hand motions observed in key grasp types. Using the MediaPipe Hand Landmarker [97], we track joint positions as users perform each grasp in free space, without an object. This data is then mapped to finger kinematics, providing a basis for designing grasp strategies that align with natural human motion. To simulate the motion of the soft robotic gripper, we adopt the friction-aware kinematic model developed for cable-driven soft robots [71]. This model builds on the pseudo-rigid body framework, representing the soft finger as a sequence of rigid segments connected by V-groove joints (Fig. 4.2), each approximated as a torsional spring. The torque at each joint J_j is calculated as the cross product between the moment arm r_{2j+1}–the distance from the joint to the cable path–and the perpendicular component of the cable tension T_{2j}, representing the mechanical leverage applied

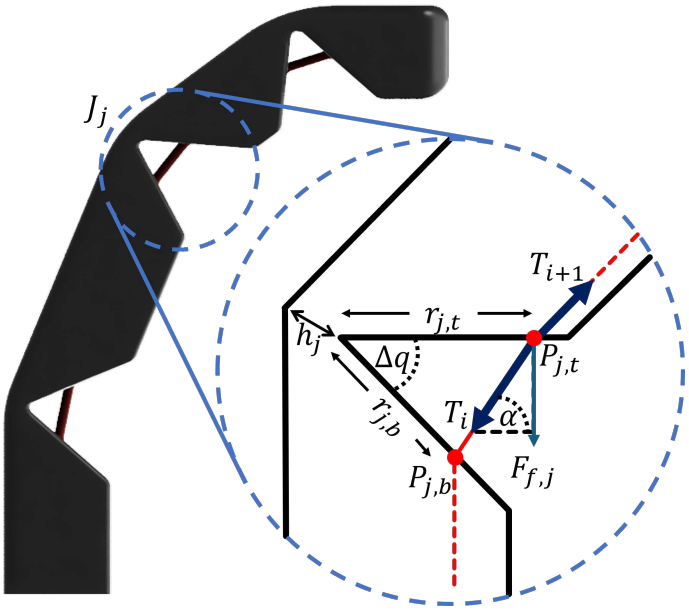

FIGURE 4.2: Annotated diagram of a soft robotic joint showing the cable routing points, cable tensions T, distances from the routing points to the joint r, joint thickness h, and joint deflection angle θ.

by the tendon force at that point. A key aspect of the model is its friction-aware capability, which accurately accounts for cable tension loss at each routing point. These routing points represent the entrance and exit positions of the tendon at each joint, associated with distances $\{r\}$. At a given routing point (e.g., at r_{2j+1}), the frictional force is expressed as the difference in cable tensions before and after the joint: $F_{f,2j+1} = T_{2j} - T_{2j+1}$. Cable friction across a deflection point is typically modeled by a tension ratio : $T_{2j} = R_f T_{2j+1}$. The friction model governing this interaction is expressed as:

$$R_f(\phi, T_{2j+1}) = e^{\mu_e \phi + \epsilon - \lambda \ln(T_{2j+1})} \tag{4.1}$$

where

$$\mu_e = \alpha(\frac{r}{T_{2j+1}})^{1-n}(\frac{\ln(1+\zeta)}{\zeta}), \text{ with } \zeta = -\alpha(1-n)(\frac{r}{T_{2j+1}})^{1-n}\phi$$

This model takes into consideration of the deflection angle (ϕ) of the cable over a surface, the asperity behaviours of both the cable and the surface. It employs an effective friction coefficient μ_e defined by parameters α and n for cable asperity, and ϵ and $\lambda \ln(T_{2j+1})$ for surface asperity reduction. In this work, the friction surface is TPU and the cable is a generic braided fishing line. Following the calibration procedure [71], their values are obtained via nine experimental tests: $\alpha = 0.27049$,

$n = 0.82038$, $\epsilon = 0.06483$, and $\lambda = 0.00851$, with an average error of 1.12% and an R^2 of 0.987.

While prior work [71] assumed a linear stiffness for each joint, TPU exhibits hyperelastic behavior, with its tangent modulus decreasing by approximately 82% under 45% strain [94]. To account for this nonlinearity, we express Young's modulus as a strain-dependent function:

$$E(\epsilon) = a\epsilon^2 + b\epsilon + c$$

where $a = 110.08$ MPa, $b = -89.33$ MPa, and $c = 21.89$ MPa. In addition, strain varies across the joint height under bending:

$$\epsilon(y) = \kappa \cdot y$$

where κ is the curvature and y is the distance from the neutral axis. Therefore, unlike the previous work [71] that assumed a constant spring stiffness, we derive the effective torsional stiffness by integrating the stress-induced moments across the cross-sectional area:

$$K_j = \frac{w}{l} \int_{-h_j/2}^{h_j/2} E(\epsilon(y)) y^2 dy, \tag{4.2}$$

where w, h_j, and l represent the width, height, and length of joint j, respectively–with w and l remaining constant across all joints. Expanding this, we derive:

$$K_j = \frac{w h_j^3}{4l} \left(\frac{a\kappa^2 h_j^2}{20} + \frac{c}{3} \right) \tag{4.3}$$

This formulation enables dynamic estimation of joint stiffness during actuation, allowing the model to accurately predict the strain and response of the soft robotic fingers under different grasping conditions.

4.2.3 Trajectory-Aware Optimization

The objective of the optimization is to design a soft robotic finger that can accurately replicate the deformation path–and thus the grasping strategy–captured from a human demonstration, while simultaneously minimizing the required actuation force to ensure an efficient and practical design. As illustrated in Fig. 4.3, this is achieved through two

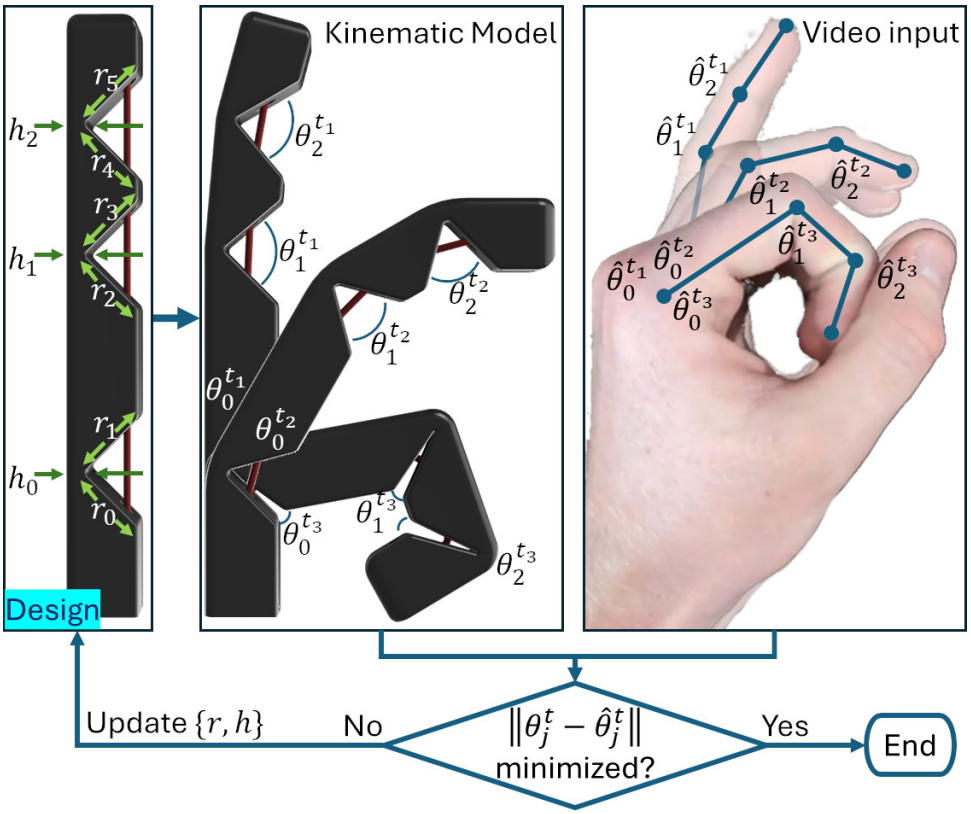

FIGURE 4.3: Joint thicknesses h and cable distances r are design variables used to tune the soft finger's deformation θ_j^t to match the target user trajectory $\hat{\theta}_j^t$.

key design variables: First, by tuning the joint thickness h_j, which directly influences the torsional stiffness K_j of each joint. Second, by adjusting the cable routing point locations, defined by distances r_{2j} and r_{2j+1}, which control the moment arm through which the cable force generates torque at each joint. Together, these parameters define how the finger deforms under actuation, and thus how closely it mimics the intended motion.

Following methods similar to prior work [72, 73], human grasp trajectories are recorded via video, capturing representative motions for each grasp type. Using the Hand Landmark Detection feature in MediaPipe Studio [97], the Cartesian positions of hand joints are extracted frame by frame. To make the optimization process independent of specific finger geometry and reduce computational complexity, this data is transformed into joint space. For each joint, a pair of vectors is formed: one from the previous landmark to the joint, and another from the joint to the next landmark. The joint angle θ_j is then computed via the dot product between these vectors. By

assuming each joint behaves as a pure revolute joint, bending in only one direction, the system is reduced to a single degree of freedom per joint. This significantly simplifies the optimization problem, reducing the number of variables by half compared to working in Cartesian space (where both x and y coordinates would be required), and thereby enhancing optimization speed and efficiency.

The optimization process is designed to balance two key objectives: trajectory fidelity and actuation efficiency. The primary goal is to ensure that each joint achieves the correct angular deformation at each stage of the finger's motion. This is quantified using the trajectory error E_T, which measures the deviation between the simulated joint angles θ_j^t, computed using the kinematic model in Sec. 4.2.2, and the target joint angles $\hat{\theta}_j^t$ over n time steps:

$$E_T = \sqrt{\frac{1}{3n}\sum_{t=0}^{n-1}\sum_{j=0}^{2}(\theta_j^t - \hat{\theta}_j^t)^2} \tag{4.4}$$

The second objective is to minimize the required actuation force, defined simply as $E_F = F_a$, where F_a is the force applied at the base of the actuation cable. The overall cost function is expressed as a weighted sum of these two objectives:

$$min(E) = \omega_1 E_T + \omega_2 E_F \tag{4.5}$$

Here, ω_1 and ω_2 are weighting coefficients that determine the relative importance of trajectory accuracy versus force efficiency. In this study, trajectory fidelity is prioritized, and the weights are set to $\omega_1 = 2$ and $\omega_2 = 1$. The optimization framework is implemented in Python, using the 'SciPy.optimize' library. The Sequential Least Squares Programming (SLSQP) method is selected for its ability to handle nonlinear constraints and bounds. The kinematic model serves as the simulation engine that relates design parameters to finger motion and force requirements. To ensure anatomical plausibility and manufacturability, the design space is bounded: joint thickness h is constrained between 2.5 mm and 5 mm, and the cable offset distances r are limited to the range of 5 mm to 13 mm.

It is important to note that the problem is highly nonlinear and multi-objective.

While increasing compliance (by reducing joint stiffness) reduces the required actuation force, it simultaneously exacerbates frictional losses, particularly at joints farther from the actuator. This creates a trade-off where optimizing for lower actuation force can negatively affect trajectory accuracy, especially due to the cumulative frictional effects along the tendon path. These competing dynamics highlight the complexity of designing efficient yet accurate soft robotic fingers, and the importance of incorporating both mechanical and actuation behavior into the optimization process.

4.3 Results

The human demonstration data was captured using a Google Pixel 8 smartphone, and the hand landmarks, including joint positions, were extracted using the Hand Landmark Detection feature in MediaPipe Studio on a desktop computer equipped with a 12th Gen Intel i7-12700K processor and 32 GB of RAM. The parametric model of the gripper was created in Fusion 360, utilizing the Parameter I/O add-in to automatically import design parameters from a CSV file. A custom Python script, developed in PyCharm, was used to perform the finger kinematics calculations, execute the optimization process, and update the CAD geometry accordingly. The gripper components were fabricated using a Prusa Mk3S FFF 3D printer equipped with a Hemera extruder. The fingers were printed from flexible TPU (NinjaFlex, 85A Shore hardness) to ensure compliant grasping, while the palm was printed from rigid PLA to provide a stable base for actuation. To minimize friction and enhance tendon routing, the fingers were printed with layer lines aligned to the cable sliding direction. The tendons themselves were made from 0.25 mm polyethylene braided fishing line, selected for its flexibility and tensile strength. For experimental validation, finger actuation was performed using an ESM 750 tensile test machine, enabling precise position control and consistent actuation speed. This setup ensured repeatable deformation measurements and accurate comparisons between optimized trajectories and physical performance

4.3.1 Optimized Finger

As detailed in Section 4.2.2, natural human hand motions serve as a foundation for designing soft grippers that closely replicate human grasping behavior. To this end,

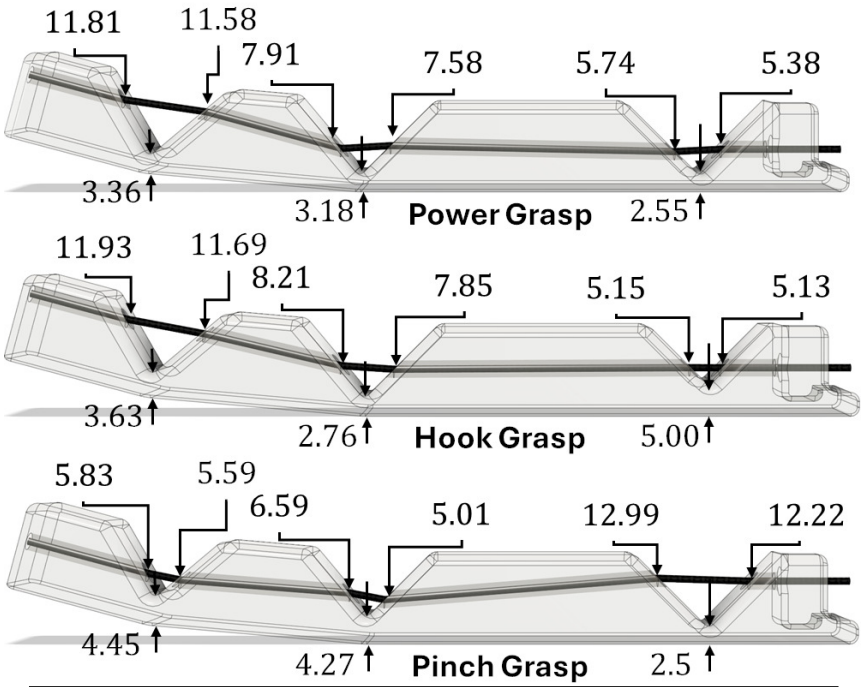

Parameter	Power Grasp	Hook Grasp	Pinch Grasp
h_0	2.55	5.00	2.50
h_1	3.18	2.76	4.27
h_2	3.36	3.63	4.45
r_0	5.38	5.13	12.22
r_1	5.74	5.15	12.99
r_2	7.58	7.85	5.01
r_3	7.91	8.21	6.59
r_4	11.58	11.69	5.59
r_5	11.81	11.93	5.83

FIGURE 4.4: Optimized finger parameters for the power, hook, and pinch grasps. h represents joint thickness, and r denotes the cable's distance from the joint. All dimensions are in mm.

the user was asked to perform the three key grasp types in free space. Figure 4.5 illustrates representative snapshots captured at three distinct moments (start, midpoint, and near completion) during each grasping motion. Additionally, the corresponding deflections of the index finger's three joints–proximal (J0), middle (J1), and distal (J2)–are plotted in solid lines against the total joint deflection (J0 + J1 + J2). Clear distinctions among the grasp types emerge from these plots. In the power grasp, all joints flex simultaneously and uniformly. In contrast, the hook grasp primarily involves deformation of the distal and middle joints, with minimal movement of the proximal joint. Lastly, the pinch grasp mainly engages the proximal joint (J0), with

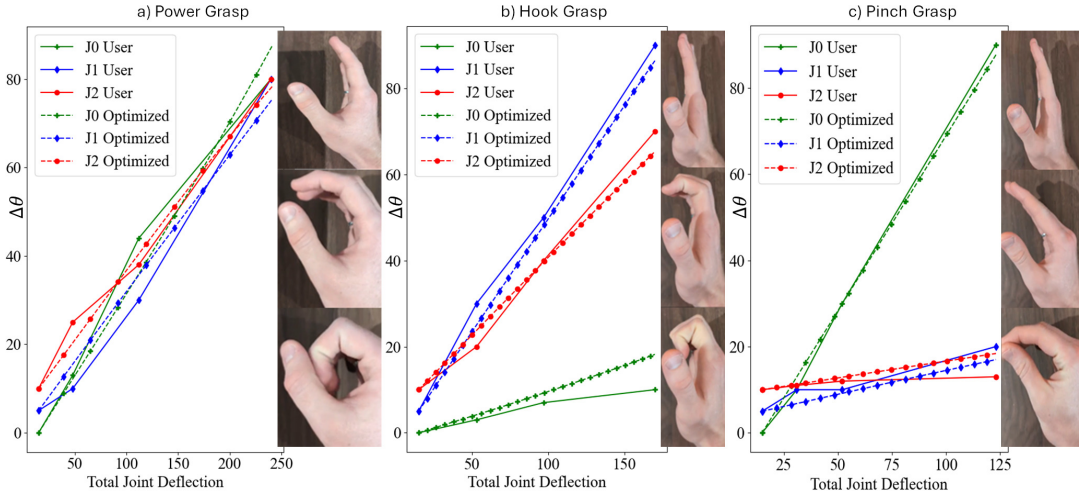

FIGURE 4.5: Comparison of joint deflection between the recorded human grasp (solid lines) and the optimized finger motion (dashed lines) for (a) Power grasp, (b) Hook grasp, and (c) Pinch grasp. J0, J1, and J2 represent the proximal, middle, and distal joints, respectively. The accompanying images show snapshots of each grasp at three key moments, from top to bottom: start, mid-motion, and final grasp.

significantly smaller deflections observed in the middle and distal joints. These characteristic joint behaviors closely align with those observed during grasping interactions with actual objects.

The optimization framework presented in Section 4.2.3 was subsequently applied to refine each finger design by adjusting the cable routing paths and joint thicknesses, ensuring that the resulting deformation closely matched the recorded human trajectories while minimizing the required actuation force. The resulting optimized finger designs, along with their corresponding parameter values, are presented in Fig. 4.4. Figure 4.5 illustrates the performance of these designs, where the solid lines represent the joint angles extracted from human demonstration, and the dashed lines correspond to the simulated trajectories of the optimized soft fingers. Overall, the optimized fingers exhibit strong alignment with the human motion data. However, a noticeable deviation occurs in the proximal joint (J0) during the hook grasp, where the trajectory diverges beyond a total joint deflection of approximately 100°. In the human data, J0 shows a sudden reduction in deformation rate at this point–an effect that the optimized finger cannot reproduce due to the system's single-point cable actuation, which lacks the ability to modulate force distribution dynamically along the finger. Additionally, the

human joint deflection trajectories display non-uniform and fluctuating rates of motion, likely due to natural inconsistencies in human grasping behavior or inaccuracies in landmark tracking. For example, in the power grasp, the proximal joint (J0) initially deforms rapidly up to 45°, then slows down, while the distal joint (J2) shows a pattern of quick deformation, followed by a showdown and a second rapid increase. In contrast, the optimized joint angles follow smooth, continuous curves, reflecting the effects of constant, linear cable actuation. Despite these differences, the optimized finger trajectories remain remarkably close to the target paths, particularly given the simplicity of the single-tendon actuation system. This demonstrates the capability of the model to effectively approximate complex human motion using a computationally efficient and physically realizable design. Quantitatively, the trajectory errors (E_T) for the optimized fingers were 6.59 for the power grasp, 5.53 for the hook grasp, and 3.76 for the pinch grasp.

Additionally, we observe similar deformation patterns across fingers within each grasp type, allowing us to generalize the optimized finger design across multiple fingers without recalculating for each one individually. This approach ensures design uniformity while significantly reducing computational complexity. However, the thumb exhibits distinct behaviours that depend explicitly on the grasp type. While its deformation patterns in the power and pinch grasps are similar, the critical difference is its interaction with other fingers. Specifically, during the power grasp, the thumb flexes without directly contacting other fingers, whereas, in the pinch grasp, it actively engages with them to form a precise and stable grip. Recognizing these subtle distinctions allows targeted customization through minor design adjustments rather than extensive recalibration. This maintains simplicity in the overall gripper design and fabrication, while ensuring optimal performance for each grasp strategy.

4.3.2 Physical Validation

To validate the proposed optimization approach, an optimized finger for each grasp type was 3D-printed and experimentally tested to confirm its ability to replicate the intended trajectories and deformation patterns. For accurate tracking, small green markers were positioned at the apex of each joint, with an additional marker placed

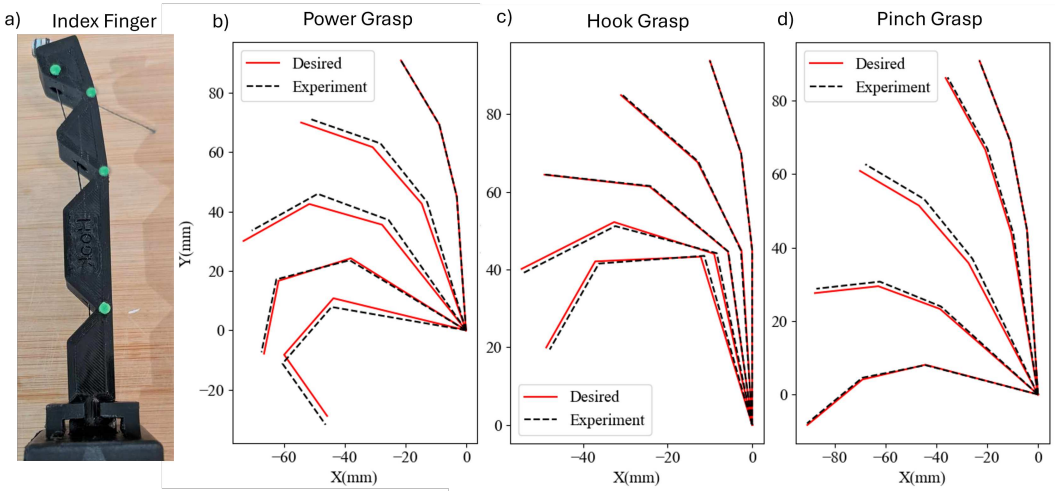

FIGURE 4.6: Comparison of 3D printed optimized finger against recorded inputs. a) Example of 3D printed soft robotic finger with markers for deformation mapping; b) Power grasp, c) Hook grasp, and d) Pinch grasp.

at the fingertip, as illustrated in Fig. 4.6a. During testing, each finger was actuated using a linear stage, and the resulting deformation was captured through video recordings. These videos were subsequently processed to isolate and track the markers' positions throughout the actuation cycle. Figures 4.6b, c, and d present a direct comparison between the experimentally measured finger trajectories and the target deformation paths derived from the original human demonstration data. Quantitative analysis showed close agreement between the experimental outcomes and the desired trajectories. Specifically, the power grasp exhibited an average error of 3.16% with a maximum deviation of 5.67%. The hook grasp yielded even better precision, showing an average error of 0.69% and a maximum deviation of 1.50%. Similarly, the pinch grasp demonstrated high accuracy, with an average error of 1.44% and a maximum deviation of 3.73%. The results from this validation indicate that more complex grasps–those involving multiple joints and larger displacements–tend to exhibit slightly increased errors. Nevertheless, the overall performance across all grasp configurations confirms that our modeling and optimization approach effectively predicts and replicates realistic finger motions. Thus, the presented method provides a robust and versatile tool for designing and accurately fabricating soft robotic grippers tailored to various grasping strategies.

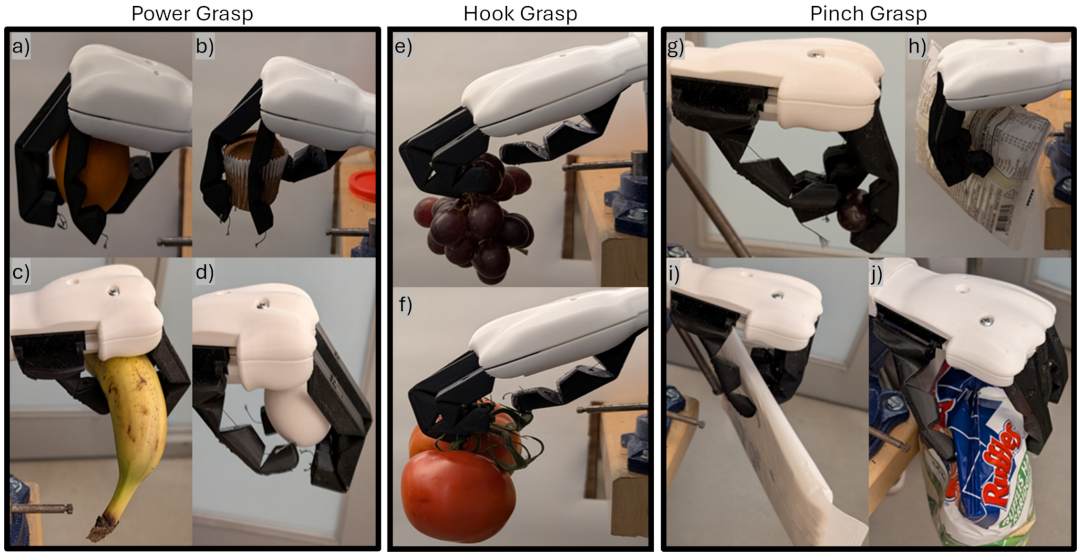

FIGURE 4.7: Images showing the gripper performing grasps on various objects using the three identified strategies. On the left, the power grasp is demonstrated with (a) an orange, (b) a muffin, (c) a banana, and (d) an egg. In the center, the hook grasp is shown handling (e) a grapevine and (f) a tomato vine. On the right, the pinch grasp is used to hold (g) a grape, (h) a sealed cheesecake, (i) a cracker sheet, and (j) a bag of chips.

4.3.3 Hand Verification

To verify the functionality and adaptability of the assembled soft robotic gripper, experimental tests were conducted using representative food items grouped into grasp-based product mixes (Table 4.1). These product mixes were determined by observing and analyzing natural human grasping behaviors, enabling the robotic gripper to closely replicate realistic hand motions and grasp strategies. During testing, each grasp type–power, pinch, and hook–was evaluated using objects specifically selected to match their respective handling categories. The experiments assessed the gripper's ability to securely grasp objects with varying geometries, textures, and fragility. A successful grasp was defined by two criteria: first, securely picking up the object without slippage or damage; second, maintaining a stable hold for a defined period (approximately 5 seconds).

The **power grasp** configuration was experimentally tested using sphere-like (e.g., egg, orange, muffin, apple) and cylindrical objects (e.g., sausage, banana, baloney), with some examples illustrated in Fig. 4.7a-d. The robotic hand consistently demonstrated simultaneous and uniform joint deformation, accurately replicating the trajectories derived from human grasp demonstrations. Across all tested objects within

this grasp category, the hand reliably achieved secure and stable grips, closely aligning with intended grasping patterns. These results confirm the gripper's capability to effectively handle diverse product geometries, demonstrating its adaptability and robustness within the power grasp category. For the **hook grasp**, validation experiments involved handling items characterized by elongated, irregular, or thin profiles, such as grape vines and tomato vines, as shown in Fig. 4.7e–f. During these tests, the robotic gripper precisely reproduced the intended deformation pattern, predominantly involving the distal and middle joints. It successfully grasped and maintained stable contact at the targeted gripping points. A key observation is that grasping success depends not only on the final joint configuration but also on the actuation trajectory leading to it. Precise, controlled sequencing of distal and middle joint flexion was essential to achieving a stable grip. Any significant deviation in actuation timing or path could have resulted in premature closure at the distal joint or unintended contact, potentially displacing or damaging the objects before establishing a stable grip. This reinforces the importance of trajectory-aware grasping, where the sequence and manner in which the fingers close are just as critical as the final grasp posture. These experimental results highlight the gripper's ability to achieve accurate, fingertip-focused manipulation, confirming its suitability and effectiveness for handling objects requiring precise and selective joint flexion. Finally, the **pinch grasp** configuration was evaluated using delicate or flat items, such as grapes, eggs, cheese slices, cracker sheets, and frozen pizza (examples shown in Fig. 4.7g-j). The gripper successfully exhibited the intended deformation pattern, primarily concentrating joint flexion at the proximal joint to achieve gentle yet secure grips. Experimental results demonstrated reliable manipulation, as the gripper accurately grasped and held all targeted food items. The only exception was the frozen pizza, weighing approximately 695 g with a slick, challenging surface. Although the gripper initially grasped this item successfully, the combination of significant weight and slippery surface texture led to reduced grasp stability, making sustained holding difficult. This highlights potential limitations of the pinch grasp configuration when handling heavier or particularly challenging objects, pointing to future areas for refinement.

These experimental results confirmed that the assembled soft robotic hand successfully replicated the intended grasp types, demonstrating adaptability and versatility

across various product mixes. The gripper consistently reproduced the target grasp trajectories derived from human demonstrations, effectively handling objects with diverse shapes, textures, and sizes. Although minor deviations occurred in grasps involving heavier or challenging items, overall performance verified the robustness and practical applicability of the design. These validation outcomes highlight the effectiveness of our design and optimization pipeline, providing a clear pathway toward modular, adaptable, and cost-effective soft robotic grippers optimized specifically for grasp-based food-handling applications.

4.3.4 Time Statistics

The proposed design pipeline significantly accelerates the translation of real-world human grasping motions into optimized, fully functional 3D-printed soft robotic hands. By leveraging a modular palm structure and parametrically optimized fingers, this approach greatly reduces the iterative design time traditionally associated with soft robotic gripper development. From input motion capture to a fully fabricated gripper, the streamlined pipeline allows efficient production. The process begins by capturing human grasp trajectories, followed by processing and analyzing the recorded motion data to extract joint movement patterns. This entire capturing and analysis phase is completed within a few minutes, after which the extracted trajectories are used to generate optimized finger designs. The subsequent optimization process for each finger, including updating the parametric model in Fusion 360, takes approximately 5 minutes. Each finger is then 3D-printed individually, requiring approximately 3.5 hours per finger. The thumb, due to its increased complexity and additional support structure requirements, takes approximately 5 hours to print. The palm component, printed separately in rigid PLA material, requires approximately 3 hours. Following fabrication, the modular design allows for quick assembly, with the entire hand constructed and ready for use in approximately 5 minutes. In total, the entire production–from grasp data acquisition and optimization to physical fabrication and assembly–can be completed under 24 hours. Notably, since all grasp-based configurations utilize a common palm structure and standardized interfaces, subsequent grippers can be produced in under 15 hours by reusing existing designs and manufacturing only the necessary finger modules.

TABLE 4.2: Grasping results for the three different grasps on all objects. ✔ represents a success, ● represents partial success, and ✘ represents failure to grasp.

Mix	Objects	Power Grasp	Pinch Grasp	Hook Grasp
Power	Egg	✔	✔	✘
	Orange	✔	✔	✘
	Muffin	✔	✔	✘
	Apple	✔	✔	✘
	Sausage	✔	✔	✔
	Banana	✔	✔	✘
	Baloney	✔	✘	✘
Pinch	Grape	✘	✔	✘
	Cheese Slice	●	✔	●
	Cheese Cake	✔	✔	✘
	Cracker Sheet	✔	✔	✘
	Frozen Pizza	✘	●	✘
	Bag of chips	✔	✔	✘
Hook	Tomato Vine	✔	✔	✔
	Grape Vine	✔	✔	✔
	Success Rate:	80%	87%	20%

Additionally, similar to the tool-changing processes in CNC machining centers, switching between grasp configurations can be performed either automatically or manually in approximately 5 minutes. Users can quickly swap fingers by simply opening the modular palm, removing the current fingers, inserting the new ones into their corresponding slots, and securing them without additional adjustments. This capability enables practical implementation in dynamic production lines that require rapid transitions between different product mixes or grasp types, significantly enhancing manufacturing flexibility and efficiency.

4.4 Discussion

4.4.1 Cross-Mix Grasping Performance

To assess the versatility, adaptability, and robustness of the robotic gripper, we evaluate whether a grasp strategy optimized for one set of objects can effectively manipulate items outside its originally intended category. For instance, testing whether a power grasp can successfully handle objects typically classified under the pinch grasp category. This cross-category evaluation helps determine the flexibility of each grasp

strategy and whether a single gripper configuration can accommodate multiple product mixes. By identifying overlaps in grasp effectiveness, this approach can potentially minimize the need for frequent gripper reconfigurations, improving efficiency in real-world applications.

Table 4.2 summarizes the performance of each grasp strategy across the tested objects. The trials reveal that the hook grasp was the least versatile, successfully grasping only three items, achieving a success rate of 20%. While it provided the most secure and stable hold for the objects it could grasp, it required precise orientation for some items, such as the cheese slice, where grasping success depended on specific positioning. This highlights the trade-off between specialization and versatility—while the hook grasp excels at specific tasks, it lacks adaptability for broader applications. The pinch grasp demonstrated the highest success rate at 87%, failing only with the baloney and frozen pizza. The baloney (70 mm in diameter, sealed in plastic film) was too large to establish sufficient contact points and too slippery for a secure grip. The frozen pizza posed challenges as only the fingertips made contact, failing to generate enough friction for a stable hold. Despite these two cases, the pinch grasp proved highly effective for most objects, particularly small and delicate items. The power grasp achieved a success rate of 80%, effectively handling most items but struggling with the grape and cheese slice. The grape was relatively too small for a power grasp, making it difficult for the gripper to achieve sufficient enclosure. The cheese slice, while graspable, exhibited partial success due to its soft and pliable texture, which often caused deformation when gripped, reducing grasp stability.

These findings highlight the trade-offs between grasp specialization and generalization in robotic manipulation. While specialized grasps, such as the hook grasp, provide superior stability for specific objects, they lack the versatility needed for handling a broader range of items. In contrast, more adaptable grasp strategies, such as the pinch and power grasps, can accommodate a wider variety of objects but still require further refinement to effectively handle edge cases involving size constraints, surface friction, and material compliance. A closer analysis reveals distinct performance differences between these grasp types. The power grasp successfully handled objects that the pinch grasp struggled with, such as baloney, which required a firm and encompassing hold. Conversely, the pinch grasp effectively manipulated items

that the power grasp failed to secure, such as grapes, which were too small for the rigid power grip to enclose properly. However, for all objects that the hook grasp successfully handled, either the power or pinch grasp was also able to achieve a stable hold. This suggests that the hook grasp does not provide unique advantages and may be redundant in this product mix. These insights underscore the importance of selecting the appropriate grasping strategies based on the task at hand. While maintaining a diverse set of grasping modes can improve overall system performance, minimizing redundancy and focusing on versatile and adaptable grasp strategies can enhance efficiency and streamline robotic gripper designs for practical, real-world use cases.

4.4.2 Modular Adaptability and Industrial Applications

The experimental validation of the soft robotic gripper provides key insights into the interplay between grasp strategies, modular adaptability, and industrial scalability. By categorizing objects into a grasp-based product mix, we demonstrated that a small set of optimized grasp types can accommodate a wide range of food products. This reinforces the principle of functional grasp redundancy, where rather than striving for a single universal gripper, a multi-gripper framework with specialized, interchangeable designs presents a more efficient and scalable alternative for robotic handling in industrial applications. A major advantage of this approach is the rapid interchangeability of grippers, allowing for grasp-type transitions in approximately five minutes. This capability is particularly valuable in automated food handling and packaging systems, where production lines frequently switch between different product types. The ability to swap grippers without requiring mechanical reconfiguration or complex reprogramming ensures minimal downtime, making this method highly compatible with dynamic, high-throughput manufacturing environments. Unlike conventional robotic grippers that require customized end-effectors or software recalibration, the proposed modular system enables seamless grasp reconfiguration simply by replacing the finger modules, significantly enhancing operational flexibility.

Beyond reducing production delays, this modular approach also expands the feasibility of task-specific robotic automation. The efficiency of the grasp-based product mix framework suggests that industrial robotic handling systems could benefit from a

multi-gripper strategy, where a limited set of specialized grippers is deployed instead of attempting full anthropomorphic dexterity in a single design. This shift challenges the traditional paradigm of general-purpose robotic hands, highlighting the advantages of application-driven, rapidly deployable gripper solutions. Furthermore, the ability to fabricate and deploy new gripper configurations within 24 hours introduces exciting opportunities for on-demand customization in industrial robotics. This capability enables manufacturers to quickly adapt robotic systems to new product lines or seasonal production shifts without requiring extensive hardware modifications. The combination of rapid design iteration, modular adaptability, and efficient deployment positions this approach as a scalable, cost-effective solution for robotic automation, particularly in industries requiring highly flexible handling solutions, such as food processing, logistics, and precision assembly.

4.5 Conclusion

The food industry presents a unique challenge for robotic automation due to the high variability in product geometry, texture, and structural integrity. Unlike rigid industrial parts, food items range from standard shapes such as spheres, cylinders, and flat surfaces to irregular, delicate, and deformable structures. Traditional robotic grippers struggle with this diversity, often requiring frequent reconfiguration and human intervention to accommodate different handling needs. This work addresses these limitations by introducing a novel design pipeline that leverages human motion data, parametric optimization, and modular soft robotics to create adaptable robotic grippers capable of emulating human grasping behaviours. The proposed pipeline enables the rapid development of modular soft robotic hands by capturing human grasp trajectories, optimizing joint stiffness and cable routing paths, and fabricating the grippers via 3D printing. This approach allows for task-specific customization while maintaining low input force requirements, closely mimicking natural grasping mechanics. The interchangeable finger configurations enhance adaptability, allowing the gripper to seamlessly switch between different grasping strategies based on product handling requirements. The pipeline is also highly time-efficient, enabling the production of an

initial gripper within 24 hours and facilitating the fabrication of new configurations in under 12 hours to accommodate changes in the product mix.

To assess the effectiveness of this approach, the gripper was evaluated using 15 diverse food items, leading to the identification of three primary grasping strategies. Experimental results confirmed that individual fingers precisely followed their intended trajectories, achieving an average accuracy of 97% or higher. The fully assembled gripper was further validated through successful grasping trials, demonstrating its capability to handle a wide range of objects, from small, fragile items (e.g., 1 cm radius grapes) to larger, heavier objects weighing up to 750 g with complex geometries. These findings reinforce the gripper's adaptability, precision, and effectiveness in high-mix environments, such as food processing and packaging, where versatility and reliability are crucial. This work highlights the transformative potential of soft robotic grippers in industries requiring highly flexible, scalable, and rapid-response automation. The combination of modular design, efficient fabrication, and human-inspired grasping offers a practical and deployable solution to robotic grasping. By enabling customized gripper development at unprecedented speed, this method paves the way for next-generation automation systems capable of seamlessly adapting to evolving product requirements–a crucial capability for food handling, logistics, and beyond.

4.5.1 Future Works

Future research can explore several critical directions to further enhance the performance, reliability, and versatility of the proposed soft robotic grippers. One key area of improvement is grip strength and contact reliability, which could be addressed by integrating textured surfaces, high-friction materials, and compliant structures. For instance, incorporating micro-textures, spikes, or nails into the gripper's fingertips–similar to designs like X-limb [3]–may improve grip stability on irregular surfaces. Additionally, replacing the current NinjaFlex TPU material with higher-friction alternatives such as silicone could enhance contact adhesion and reduce slippage. Another important consideration is the 3D printing orientation of the fingers. While the current setup optimizes for manufacturing efficiency and minimal support material, the alignment of layer lines with pulling forces inadvertently reduces surface friction.

Modifying the print orientation or applying post-processing techniques (e.g., coatings or texturization) could improve grip performance without compromising structural integrity.

Another key avenue for improvement lies in optimizing grasping synergies across all fingers. Ensuring uniform cable lengths and synchronized actuation could reduce the number of actuators required, making the system simpler, more compact, and energy-efficient while preserving its functional versatility. A more refined tendon-driven mechanism could enhance force distribution, allowing for more natural and adaptive grasping behaviors. This approach aligns with the broader goal of achieving dexterous, human-like grasping with minimal mechanical complexity. The thumb's functionality is another area that warrants further refinement. While previous studies, such as Zhou et al. [96], have established baselines for thumb geometry, opening angles, and dimensions, future work should optimize thumb deflection in relation to the movement of other fingers. This is especially crucial for low-actuation designs, where a single actuator may control the entire hand. By integrating the thumb's trajectory into the global optimization process, its motion can be seamlessly coordinated with finger flexion, ensuring that all grasping strategies–from power to precision grips–are executed effectively. Additionally, exploring multi-actuation thumb designs or variable stiffness structures could further broaden the range of grasp types the gripper can accommodate.

Chapter 5

Simulation of Hyper-Elasticity by Shape Estimation

Nomenclature

χ System Energy

E Young's Modulus

$Q\Sigma D^T$ Matrices obtained by singular value decomposition

U Strain Energy

5.1 Introduction

Simulation has become an essential tool in soft robotic design, helping reduce the reliance on trial-and-error by enabling predictive modelling. However, accurately simulating the complex, non-linear behaviour of hyperelastic materials remains a major challenge, especially when real-time performance is required. Traditional methods like the Finite Element Analysis (FEA) offer high fidelity but often sacrifice speed, while faster alternatives like position-based dynamics or geometry-defined finite elements (GDFE) tend to simplify material behaviour, limiting accuracy. Recent advances in GDFE show promise by representing actuation through changes in geometry rather than updating system matrices, offering real-time performance with some trade-offs. However, these methods are typically restricted to linear material models and a limited number of material types. Motivated by this gap, this chapter explores the question: *How to express the non-linear material behaviour through the shape functions on a local level, such that the computational speed is not affected?*

To properly simulate hyperelastic materials, every element needs to be treated individually and have its corresponding stiffness. Thus the number of materials is only limited by the size and density of the mesh. Additionally, since the material properties are dependent on current deformation, the initial material ratios cannot be assumed to be constant at the start of the simulation. The shape blending method

prescribes a shape factor for each element based on relative properties, as such the shape factor of one element depends not only on their material characteristics but also on the current state of other elements. This needs to be implemented on a time-step or deformation dependent algorithm to ensure proper estimation of properties. This work proposes a novel method to address the non-linear material properties and true multi-material capability. Utilizing the GDFE framework, it is possible to translate material models into a relation between two target shapes, a rigid shape based on the previous state of the element and volume conservation of the current shape, that better reflect realistic deformation. This is done by comparing each element's rigidity relative to one another and setting a ratio between a soft configuration and hard configuration. Insight on utilizing multiple materials allows for efficient implementation of hyper-elastic material models within the framework. The contributions are:

1. A mathematical model between the shape factor and material properties is defined and calibrated, which can be applied to convert stiffness into a geometric quantity for simulation.

2. By computing the deformation's strain energy for each element, their instantaneous stiffness can be determined to obtain its corresponding shape factor in each step. Therefore, the framework can virtually work for infinite materials.

3. Hyper-elasticity is incorporated in the geometric computation by controlling each element's shape factor, allowing the global stiffness matrix to stay constant throughout and thus maintaining the fast simulation speed.

The rest of this chapter is organized as follows. Section 5.2 will outline the geometry-based approach. The methodology of hyperelasticity through geometry is discussed in Section 5.3. Finally, Section 5.4 will go over the results and validation of the chapter, followed by a conclusion in Section 5.5.

5.2 Background: Geometry-based Computing

To be self-contained and to facilitate the explanation of my developments, the geometry-based approach [30] is summarized in this section. The approach utilizes a mesh $\mathbf{M}$

which is composed of m elements and n vertices. Each element's shape, a hexahedron for this work, is described by 8 vertices stored in matrix $\mathbf{V_i}$. The subscript i represents the element to which these vertices belong. Each element has a desired shape or configuration. This is determined by a blending operation based on the material, which will be detailed later. For clarity, this blended shape will be denoted as $\mathbf{V_i^B}$ and referred to as the desired shape of an element. When constraints or forces are applied to mesh $\mathbf{M}$, they are transferred into each element, which is then deformed, increasing the energy of the system. The energy is calculated as the difference between the desired shape $\mathbf{V_i^B}$, and the current shape $\mathbf{V_i}$ defined as

$$\chi(\mathbf{M}) = \sum_{i=1}^{m} diff(\mathbf{V_i^B}, \mathbf{V_i}). \tag{5.1}$$

The algorithm tries to minimize the entire system's energy while obeying all constraints using a two-step solver. The first step is a local step where each element $\mathbf{V_i}$ is used to orient their corresponding desired shape $\mathbf{V_i^B}$. A global step then aims to solve an over-constrained linear problem.

5.2.1 Local Step

There exists a relationship between the current shape $\mathbf{V_i}$ and the desired shape $\mathbf{V_i^B}$. This step aims to solve for a rotational matrix $\mathbf{R_i}$ which can orient the element's original rigid shape $\mathbf{V_i^R}$ with the current shape $\mathbf{V_i}$, minimizing the difference in shape and energy. The equation characterizes the difference between both shapes:

$$U = \Omega_i ||\mathbf{NV}_i - \mathbf{R}_i(\mathbf{NV}_i^R)||, \tag{5.2}$$

where Ω_i represents the weight of the element based on its volume. Typically to match two elements a full transformation matrix would be required. Here, matrix $\mathbf{N}$ is used to center an element and remove the translation aspect of the comparison:

$$\mathbf{N}(i,j) = \begin{cases} 7/8 & \text{if} \quad i = j \\ -1/8 & \text{if} \quad i \neq j \end{cases} \quad \forall i,j \in (1,2,...,8).$$

$\mathbf{N}$ relates each vertex to one another. In this sense, it is possible to compare the $\mathbf{N}$ matrix to a traditional FEM local stiffness matrix. The transformation matrix $\mathbf{T}$

can then be reduced to a simple rotation and scaling matrix. Considering there are 8 vertices in an element, the problem is over-constrained and can be solved by the least squared method to obtain the affine transformation, including both the scaling and rotation elements. Since the blended shape will enforce the scaling, the only characteristics of interest in $\mathbf{T}$ are the rotational properties. These can be found through singular value decomposition (SVD). This results into $SVD(\mathbf{T}) = \mathbf{Q}\Sigma\mathbf{D}^{\mathbf{T}}$, where $\mathbf{Q}$ and $\mathbf{D}$ are the rotational components and Σ is the scaling matrix. Matrix $\mathbf{R_i}$ from Eq. 5.2 can then be defined as $\mathbf{R} = \mathbf{Q}\mathbf{D}^{\mathbf{T}}$, keeping only the rotational elements. Multiplying $\mathbf{R}$ with $\mathbf{V_i^R}$ determines the rigid configuration used in the shape blending process to determine the desired shape $\mathbf{V_i^B}$.

5.2.2 Global Solve

The summation of all the local steps creates an over-constrained system of linear equations that can be efficiently solved for shown by this equation:

$$\chi = \sum_{i=1}^{m} \Omega_i ||\mathbf{N}\mathbf{V_i} - \mathbf{R}(\mathbf{N}\mathbf{V_i^B})|| = ||\mathbf{A}\mathbf{V} - \mathbf{p}||. \tag{5.3}$$

$\mathbf{V}$ is a 3D vector of all the current position of all vertices in the mesh, while $\mathbf{p}$ is a 3D vector of the local solutions for each element. Equation 5.3 can be solved iteratively [92] by firstly constraining $\mathbf{V}$ and solving for $\mathbf{p}$, and then constraining $\mathbf{p}$ and solving for $\mathbf{V}$. This leads to a least square problem in the form of $\mathbf{A}^{\mathbf{T}}\mathbf{A}\mathbf{V} = \mathbf{A}^{\mathbf{T}}\mathbf{p}$. It is to be noted that matrix $\mathbf{A}$ is composed of solely matrix $\mathbf{N}$, which means it is constant. This allows for the matrix $\mathbf{A}^{\mathbf{T}}\mathbf{A}$ to be precomputed at the start of the simulation, making it extremely efficient. Additionally, where typical FEM requires a $3n \times 3n$ for $\mathbf{A}^{\mathbf{T}}\mathbf{A}$, this approach is only $n \times n$ since each axis can be solved individually using the same global matrix. These two properties are part of the reason why this method is attractive for simulation.

5.2.3 Shape Blending

The geometry-based formulation allows for setting a target shape $\mathbf{V_i^B}$ for each element. In some instances, like as rigid as possible (ARAP) [89], an element will try to stay rigid or similar to its original shape. In others, they might mimic a smart

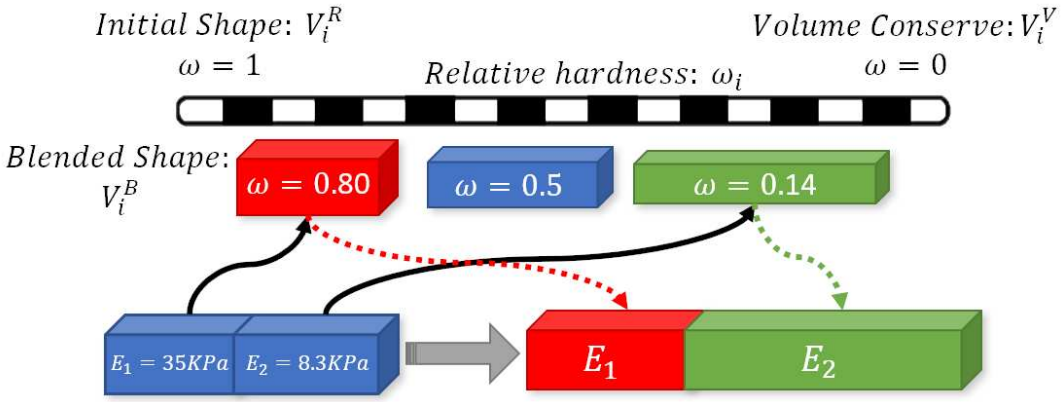

FIGURE 5.1: Visualization of physical properties with relation to shape factor. A larger shape factor results in less deformation, similar to having a larger Young's Modulus.

material where they change shape to mimic deformation of a shape memory polymer (SMP) [98]. When there are two different materials in consideration, an element's stiffness is formulated based on how much it cares about its original shape compared to simply conserving its volume. As such, if one element cares about its original shape more than another, it will better maintain its shape during the energy minimization process. In the work of Fang *et al.* [30], two materials were stretched using a tensile test. They had their relative elongation compared and fitted to a general equation which assigned their relative stiffness using a shape factor ω as depicted in Fig. 5.1.

Equation 5.4 depicts how the stiffness of an element i is defined in the geometry-based approach. If the mesh is made of a singular material all ω_i will be equal. If there are two materials, than all elements of the first material will have its corresponding ω_1, while the second material will have ω_2, both of which are determined experimentally.

$$\mathbf{V_i^B} = \omega_i * \mathbf{V_i^R} + (1 - \omega_i)\mathbf{V_i^v}. \tag{5.4}$$

Figure 5.2 depicts the reasoning behind this approach. Suppose the total strain energy $\mathbf{U}$ given a certain elongation is determined. In that case, it could be reasoned that under uniform loading conditions, two materials with different stiffness would take an equal part in dividing the total strain energy when simulated together $U_T = U_S + U_R$. As such, a rigid material that is twice as stiff as a softer material should have a strain ϵ_R half as large as the other's ϵ_S, while maintaining the area under the curve equal, $U_R = U_S$.

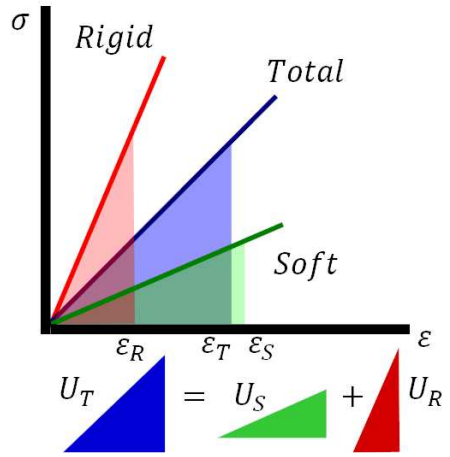

FIGURE 5.2: Multi-material strain energy formulation.

The current limitation is that the calibration method of the previous work only works for two materials. Additionally, the materials have to be linear, as the shape factor is determined and set at the start of the simulation.

5.3 Methodology

A simple visual approach to calibrating relative material properties has been developed under the assumption the materials behaved linearly [30]. This gave similar results to the real-world examples and demonstrated potential for the shape blending approach. In simple deformation cases under minimal deformation, a linear model for a single material could be used with high fidelity to define deformation. However, hyperelastic materials present non-linear mechanical behaviour and cannot be adequately defined using Hooke's law. Due to most materials used in soft robotics, e.g., exhibiting hyperelastic material properties, a new formulation and approach need to be developed to deal with non-linear material models. If the geometry-based approach can extend to make every element have its own material, then it would be possible to model hyperelasticity. However, when dealing with non-linear material models and large deformation, the global stiffness matrix typically needs to be updated to reflect the state of the deformation. This is a computationally expensive task that must be performed after every step of the simulation. Therefore, the challenge here is to accurately reflect material properties and non-linear phenomena without recomputing the global stiffness matrix $\mathbf{A}$ to ensure the performance benefits this method offers

persist.

Looking at Eq. 5.4 it can be seen that the shape factor ω can determine how rigid or soft an element is and directly dictate its stiffness. As such, introducing several materials with different shape factors ω is similar to having elements with different stiffness E, creating a link between geometry and mechanical representations. This allows tuning of an element's properties locally without touching the global stiffness matrix. A rigid element will try to maintain its previous shape during iterations, while a soft element will simply try to keep its volume; thus, its shape may change more freely. Nevertheless, another challenge is how ω should be defined when there are multiple materials. For hyperelastic materials, the stiffness of a material will change based on its current deformation. As such, the shape factor ω needs to be modified at every step to reflect the non-linear material mechanics properly. Additionally, due to the framework utilizing relative properties, the correlation between elements will have to be updated as well.

If both these concerns are addressed, then any number of materials can be simulated and easily incorporated into the framework. The only metrics that change between materials are the constants used to characterize the non-linear material models; the outputs and inputs are still the same and thus require no additional time for new materials. Two aspects are required to implement non-linear material mechanics to the framework properly:

1. Obtaining the tangent or Young's modulus of a material at any given deformation

2. Efficiently normalize the relative material properties and assign an appropriate ω

5.3.1 Capturing Hyperelasticity

Material models for hyperelastic materials typically utilize strain-energy density to describe mechanical behaviour and the relation between stress and strain. One of the unique properties of hyperelastic materials is to undergo large strains under relatively low stress and return to their original configuration with minimal plastic deformation [99]. Additionally, a hyperelastic material's properties are dependent on the

current deformation of the material [100]. As each element of a discretized model will experience different strain, a unique stiffness is required for each, resulting in different responses to loads and actuations. The phenomenon is further amplified when multiple hyperelastic materials are simulated together as their individual non-linear deformations will be based and compounded relative to one another. This necessitates a more profound understanding of the material's mechanics and how to emulate them better.

The derivation of the strain energy can be obtained by the principal stretches of the deformation gradient [101], which are then used to obtain the tangent modulus of a hyperelastic material required for geometric models. The deformation gradient tensor $\mathbf{F}$ represents all the required information for transforming an elements' initial shape to the current configuration. The determinant of $\mathbf{F}$ is the Jacobian $\mathbf{J}$ which represents the change in volume of the element. To obtain the equivalent strain of an element, the deformation gradient can be found by comparing the current shape of the element $\mathbf{V_i}$ and the initial shape $\mathbf{V_i^R}$.

The process is similar to the local step of the geometry-based framework, but the scaling matrix is of interest here, i.e., $SVD(\mathbf{F}) = \mathbf{Q}\Sigma\mathbf{D^T}$, with

$$\Sigma = \begin{bmatrix} \lambda_1 & 0 & 0 \\ 0 & \lambda_2 & 0 \\ 0 & 0 & \lambda_3 \end{bmatrix}$$

Taking the principle diagonal of the Σ matrix gives the strain tensors in each axis which are used to calculate the Von Mises equivalent strain:

$$\epsilon_{eq} = \frac{1}{(1+\nu)}\sqrt{\frac{(\lambda_1-\lambda_2)^2+(\lambda_2-\lambda_3)^2+(\lambda_3-\lambda_1)^2)}{2}} \tag{5.5}$$

where ν is the Poisson's ratio. The tangent modulus can then be obtained by taking the stress-stain curve's derivative at ϵ_{eq}. Solving for every elements' tangent modulus allows for comparing elements and calculating relative material properties, creating the inputs for the second criteria.

5.3.2 Geometric Modeling of Hyperelasticity

As mentioned in Section 5.2.3, the stiffness of an element is done within the blended shape by selecting a rigidity shape factor ω_i between a rigid shape $\mathbf{V_i^R}$ and a volume conserving shape $\mathbf{V_i^v}$. However, this is a geometric representation of stiffness with a constant global stiffness matrix. Material mechanics and physical stiffness are typically handled in a global stiffness matrix that can be updated or modified during a simulation to express non-linear phenomenons such as material properties, load distribution or large deformations. The mechanical stiffness is typically reflected through the Young's Modulus, E, of the material. However, the geometric definition of rigidity has a normalized scale from 1 for perfectly rigid, to 0 for an element that solely cares about its volume; requiring mapping to reflect the mechanical implications accurately. By that token, an element with a shape factor ω_i of 0.9 compared to an element with ω_i equal 0.1 will not perform with the naive ratio of being 9 times stiffer.

$$\Gamma(R_M) \mapsto R_G \tag{5.6}$$

The mapping function Eq. 5.6 is required for both the mechanical and geometrical stiffness to perform identically. The ratio of the two shape factors (i.e., $R_G = \omega_x/\omega_y$) corresponds to the desired ratio of its physical counterpart (i.e., $R_M = E_x/E_y$), where E_x and E_y are the Young's modulus of two theoretical materials. Once developed, the number of materials the software can handle can be endless. In this sense, hyperelastic elements can also be modelled since every element will have a unique stiffness based on its current deformation.

Mapping

The mapping process involved stretching a rectangular mesh to a pre-defined length. The left half of the mesh has one shape factor ω_{left}, and the right side has another shape factor ω_{right} assigned to it. The input $R_G = \frac{\omega_{left}}{\omega_{right}}$ was set from 1 to 90. For example, $R_G = 30$ means that the left side is 30 times stiffer than the right, which can be achieved by setting the left side to 0.9 and the right side to 0.03. After both sides have a shape factor assigned, it is stretched to 100% elongation and the equivalent strain energy of both halves are recorded. The output is the ratio between

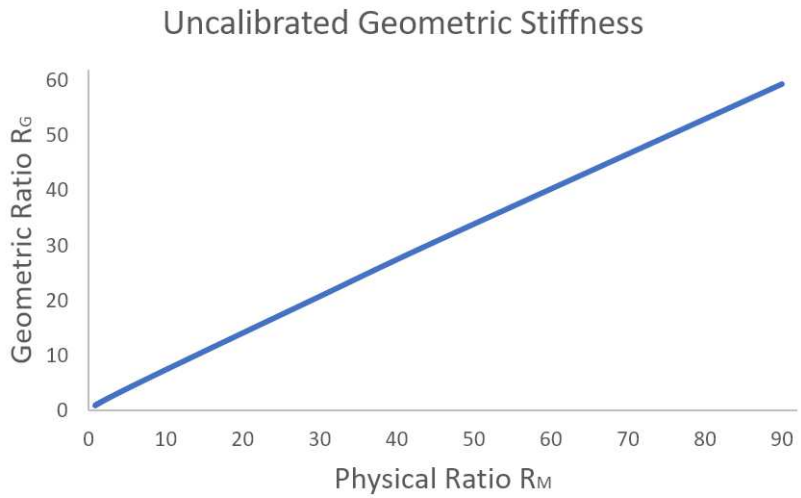

FIGURE 5.3: Calibration of Young's modulus ratio and geometric stiffness ratio.

strain energies and is equivalent to the ratio of physical stiffness R_M.The input for the mapping is R_G, and the strain energy obtained after a simulation is the output R_M. The right side's ω is modified, and the process is restarted. This generates an uncalibrated relationship between the mechanical ratios and geometric ratios for each case, that is plotted and fitted. The results of the uncalibrated simulation are shown in Fig. 5.3 and demonstrate that the geometric stiffness is stiffer than the desired mechanical response when comparing two linear materials. Comparing the geometric ratio R_G to the desired mechanical ratio R_M showed a non-linear relation between the two. Curve fitting was performed on the data to obtain a correlation. Eq. 5.7 is used to map the ratio between Young's Modulus R_M, and the equivalent geometric ratio R_G which is used for the simulation.

$$R_G = 0.0017R_M^2 + 1.42245R_M - 0.4141 \tag{5.7}$$

Elements are given their own relative stiffness ratio for the current step represented by $R_{M,i} = E_{max}/E_i$, where E_{max} is the largest tangent modulus, and E_i is the tangent modulus of an element at its current deformation. Given that the relative properties must be normalized, the maximum and minimum are identified and are at the extremities of the weighting, whose ratio between E_{max} and E_{min} is given by $r_{max} = E_{max}/E_{min}$. To center and normalize the local stiffness of elements around a

ALGORITHM 1: Hyper-Elastic Calculation

Input: The rest shape $\mathbf{V^R}$ and current positions $\mathbf{V_i}$ for investigated elements and material. Number of elements m

Output: The local stiffness ratio ω for blended shape $\mathbf{V^B}$

while $i < m$ **do**
  `/* Calculate Equivalent Strain */`
  Compute $\mathbf{F}$ between $\mathbf{V_i^R}$ and $\mathbf{V_i}$
  Apply SVD to obtain principle strains $\lambda_{1,2,3}$
  Use Eq. 5.5 to obtain equivalent strain
  Record min and max tangent modulus, $E_{i,min,max}$
end
while $i < m$ **do**
  `/* Match Stiffness Ratio */`
  Calculate minimum and maximum modulus ratio r
  Compare element E_i to E_{max}
  Solve for ω_i using Eq. 5.8
end

shape factor $\omega = 0.5$, ratio $h = r_{max}/(r_{max} + 1)$ is derived. Using the above notations and equations, the geometric shape factor ω_i for each element is calculated by

$$\omega_i = \frac{h}{R_{G,i}}, \tag{5.8}$$

where $R_{G,i}$ is obtained from the calibration Eq. 5.7. An outline of the process to compute this shape factor is presented in Algorithm 1. It is to be noted that the geometric formulation's least square problem $\mathbf{A^T A V} = \mathbf{A^T p}$ in the global step (5.2.2) has a constant global matrix $\mathbf{A^T A}$ regardless of the number of materials. The changes in the shape factor ω_i only update the right-hand side of the equation, i.e., the vector $\mathbf{p}$. This is because every element already requires its own ω_i, and all the ω_i can be the same or different with no additional computational cost. The only added computation is Algorithm 1 for non-linear materials. This step is equivalent in time to a single local solve and is only performed periodically to ensure an accurate representation of the material properties. Thus, it has a negligible impact on the overall performance.

Integration of non-linearity

Since the current rigidity is based on instantaneous deformation for hyperelastic materials, the converged deformation state of the previous step needs to be reflected in the shape blending algorithm as well. To do this, an intermediary shape $\mathbf{V_i^P}$ can be

calculated at each step to represent the previous deformation:

$$\mathbf{V_i^P} = (1-\alpha)\mathbf{V_i^R} + \alpha * \mathbf{Vi^v}, \tag{5.9}$$

which denotes the relationship between the current volume conserved shape $\mathbf{V_i^v}$ and the initial rigid shape $\mathbf{V_i^R}$. The ratio α is defined as $\alpha = \epsilon_p/\epsilon_c$, where ϵ_p is the strain of the previous step, while ϵ_c is the strain of the current shape. This allows the blending method to capture an element's state as a new reference point without overemphasizing the captured shape, thus reducing path dependency and risk of divergence. The more a shape deforms, the lower the impact of the rigid shape, but it also prevents a shape from completely diverging during an iteration as the energy will increase proportionally if it changes too much. A modified version of Eq. 5.4 incorporates the new metric. The blended shape is then defined as the shape factor ω balancing both $\mathbf{V_i^P}$ and $\mathbf{V_i^v}$ as shown below:

$$\mathbf{V_i^B} = \omega_i * \mathbf{V_i^P} + (1-\omega_i)\mathbf{V_i^v}. \tag{5.10}$$

$\mathbf{V_i^B}$ is a blend of the element's initial shape and the deformed shape. Here, α represents the instantaneous state of the element, while ω is the relative stiffness of the element. In this sense, a stiffer material will always try to maintain its shape, while the softer will care more about volume with an approximate shape. An illustration of the relationship between the shapes and physical meaning is shown in Fig. 5.4.

5.4 Results

Three tests were performed to validate the framework and its ability to simulate non-linear material properties. The first demonstrates the ability to simulate multiple linear materials simultaneously. The second experiment compared the ability of the software to simulate non-linear materials and its performance. Finally, the last experiment validated the framework's ability to simulate two 3D printed hyperelastic filaments in a tensile test while highlighting linear models' inadequacy for such material. The first and second tests are compared to an industry FEA solver Abaqus. All simulations were performed on the same machine with an Intel i7-7700HQ CPU at

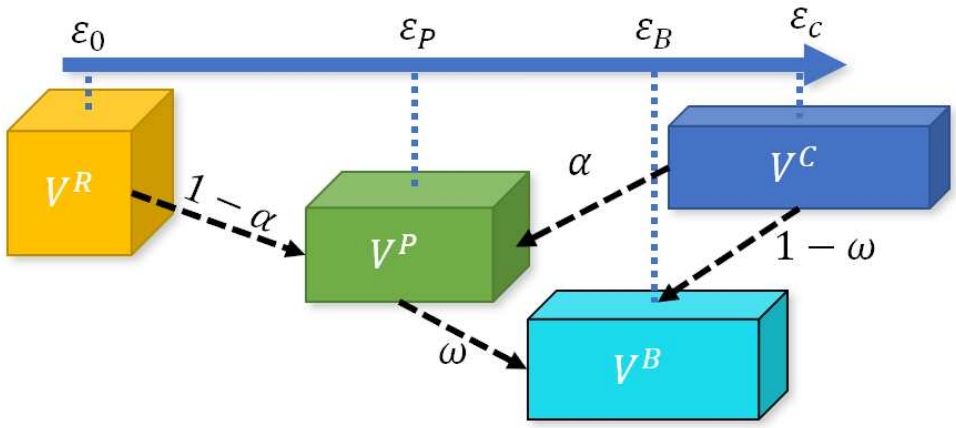

FIGURE 5.4: Visual representation of the blended shape V^B and how it is composed. The previous shape V^P is based on a composition of the rigid shape V^R and Volume preserved shape V^V.

2.80GHz, and 16GB of DDR4 RAM. The framework was coded in C++ and utilizes the open-source Eigen library [102] for solving.

The hyperelastic materials used for validation are Cheetah and NinjaFlex filaments. The physical samples were printed on an Ender 5 printer using the Flexion Extruder. The extruder is specifically designed for direct drive extrusion of flexible filaments. These filaments were then printed into a standard shape to be passed through tensile tests using the ESM 750S. These tests generated the stress-strain curves for each material. The pieces were printed at 100% infill, with 3 walls and grid infill. The printing parameters for the Cheetah were 60mm/s, at 230 degrees, while the NinjaFlex was printed at 40mm/s and 240 degrees and 105% flow. Both were printed at 0.2mm layer height. Fig. 5.5 shows the stress-strain curves for the tensile tests for both NinjaFlex and Cheetah. To capture the material properties from the stress-strain data, it is fitted to different hyperelastic models. The third-order Ogden model [103] was used to fit the data, depicted as follows:

$$W = \sum_{i=1}^{3} \frac{2\mu_i}{\alpha_i^2}(\lambda_1^{\alpha_i} + \lambda_2^{\alpha_i} + \lambda_3^{\alpha_i} - 3), \tag{5.11}$$

and the constants found for each material is listed in Table 5.1. This model is used in Abaqus to simulate hyperelastic materials. To allow a direct and simple calculation of the tangent modulus at any given strain to be used in my method, a polynomial was also fit to the test data for each material. The polynomial fitting equation for

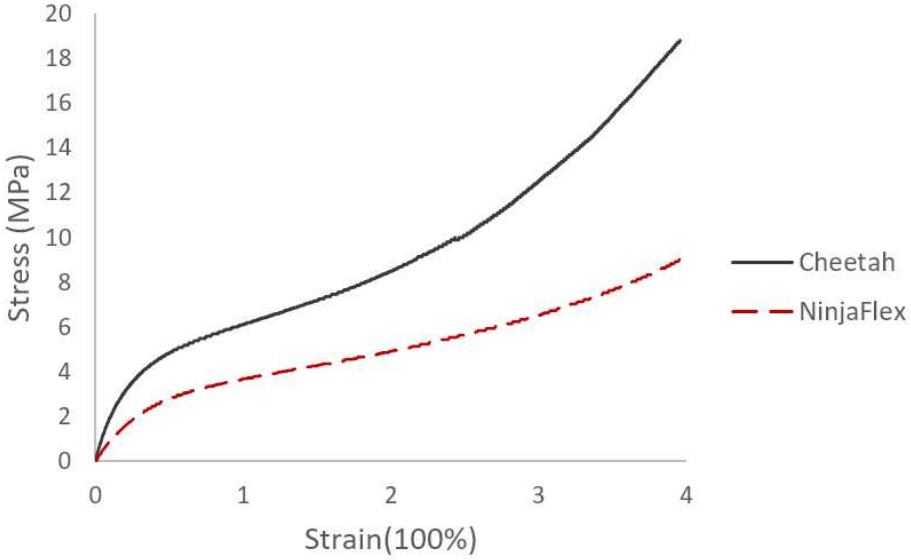

FIGURE 5.5: Stress-strain tensile test data of NinjaFlex and Cheetah filaments

TABLE 5.1: Ogden Constants for Abaqus

Constants	**NinjaFlex**	**Cheetah**
μ_0	0.187297	−5.497378
μ_1	0.091893	2.499418
μ_2	3.397167	12.259373
α_0	1.940480	3.303409
α_1	4.009788	3.722506
α_2	−1.512803	−4.762911

NinjaFlex and Cheetah are presented in the following respectively.

$$\sigma_{Ninja} = -0.13\epsilon_{eq}^6 + 1.53\epsilon_{eq}^5 - 6.91\epsilon_{eq}^4 + 15.02\epsilon_{eq}^3 - 15.7\epsilon_{eq}^2 + 8.67\epsilon_{eq}$$

$$\sigma_{Cheetah} = -0.11\epsilon_{eq}^6 + 1.49\epsilon_{eq}^5 - 7.69\epsilon_{eq}^4 + 19.9\epsilon_{eq}^3 - 26.6\epsilon_{eq}^2 + 19.13\epsilon_{eq}$$

Both the polynomial fit and the Ogden model fit the test data with high similarity. Additionally, both the geometric framework and Abaqus utilized linear Hexadra ("brick") elements.

5.4.1 Multi-material Linear Comparison

Our work proposes a new method to address multiple materials simultaneously that extends past a two material limit. This is important as hyperelastic materials, when discretized, represent individual non-linear material properties for every element,

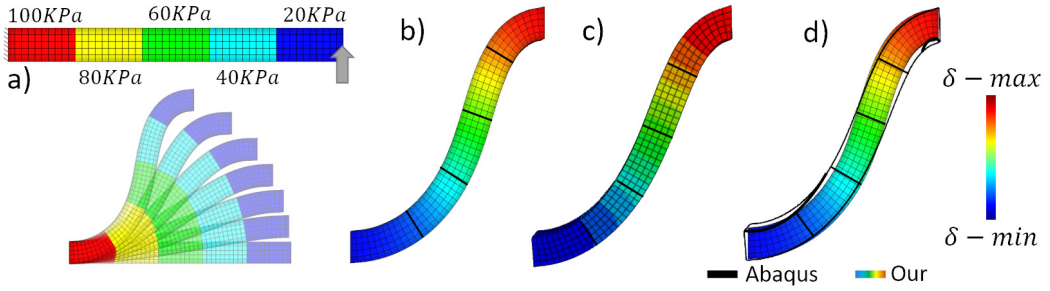

FIGURE 5.6: Multi-material validation for linear materials comparing my framework with Abaqus. a) A $50 \times 5 \times 5$ bar is displaced vertically from the right while maintaining orientation and planerity. The bar is subdivided into 5 different materials with different Young's Modulus; from left to right: 100KPa, 80KPa, 60KPa, 40KPa, and 20KPa. b) Results of my framework; c)Results from Abaqus; d)Overlaid results of my framework in color and Abaqus outlined in black.

meaning the number of elements represents the number of individual materials to be simulated. The framework is validated by simulating five different linear materials in bending and comparing it to the same simulation in Abaqus, as shown in Fig. 5.6. A bar measuring $50 \times 5 \times 5cm$ composed of 1250 elements is bounded on the left and displaced vertically on the right. The right-hand side is constrained to prevent rotation but allow horizontal displacement. The bar's material distribution, starting from the left, is: $100KPa$, $80KPa$, $60Ka$, $40KPa$, and $20KPa$; each representing a unique stiffness. The expected result is for the softer materials to exhibit more significant deformation and curl than the stiffer materials on the left. Fig. 5.6 d) shows a good correlation with the commercial software. The simulation demonstrates the ability to handle multiple materials without the need to calibrate each one individually. When comparing displacement of every node, a 3% average displacement error is observed. The Abaqus simulation took 71.4 seconds to perform, while my framework took 11.3 seconds. It is to be noted that as the deformation was increasing the convergence time for the Abaqus simulation also increased, demonstrating one of the issues with traditional FEA. Computation time in my framework stayed relatively constant throughout. Its been demonstrated, that the materials' mechanics were directly converted to geometric stiffness and into a shape factor for each material. This example could be repeated with as many simultaneous materials as desired, demonstrating new capabilities compared to previous work.

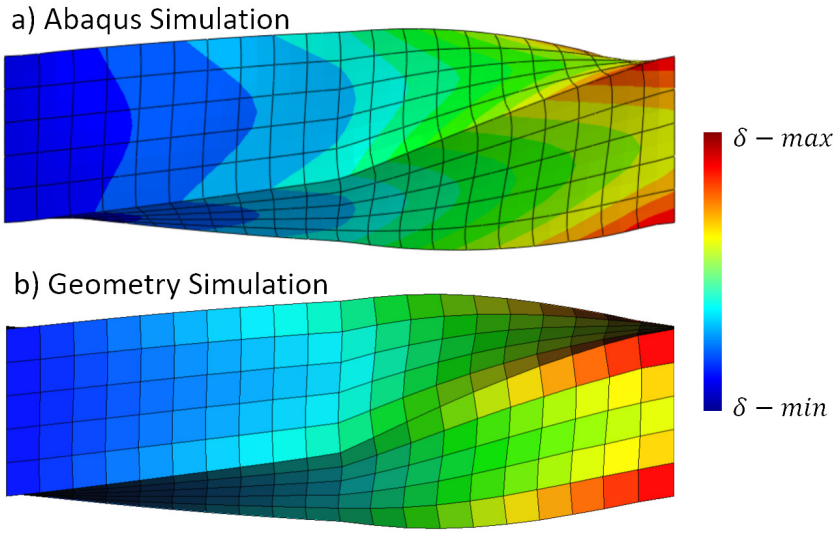

FIGURE 5.7: Rotation comparison between (a) Abaqus and (b) the framework. Left half is composed of Cheetah, right half is composed of NinjaFlex. The colors represent displacement.

5.4.2 Rotational Comparison

The geometric framework's hyperelastic capabilities were compared to Abaqus in this example. A rotation simulation shown in Fig. 5.7 was performed where the left half of a bar was characterized as Cheetah, while the right side was formed of NinjaFlex. Both simulations had a size of $20 \times 5 \times 5cm$ and an element count of 500. A 90-degree rotation of the right plane was performed in both Abaqus and the geometry-framework, matching nodes were compared to verify accuracy. An average difference in nodal placement after deformation was noted to be only 3%, with a maximum difference between both simulations of 6%. The Abaqus simulation took 19.35 seconds to perform, while my method took only 4.19 seconds. This demonstrates agreeable results between both cases, while having a significant speed increase.

5.4.3 Multi-Material Hyperelastic Tensile Test

To validate the material models and the simulation framework for hyperelasticity, a tensile test with multiple materials: Cheetah and NinjaFlex, was performed. Both specimens are joined together thermally and mechanically during the printing process and are of equivalent length. The percent elongation of both materials is measured by keeping track of the joining line between the materials using visual processing. Figure 5.8 shows the experimental set-up and results. Two simulations were performed

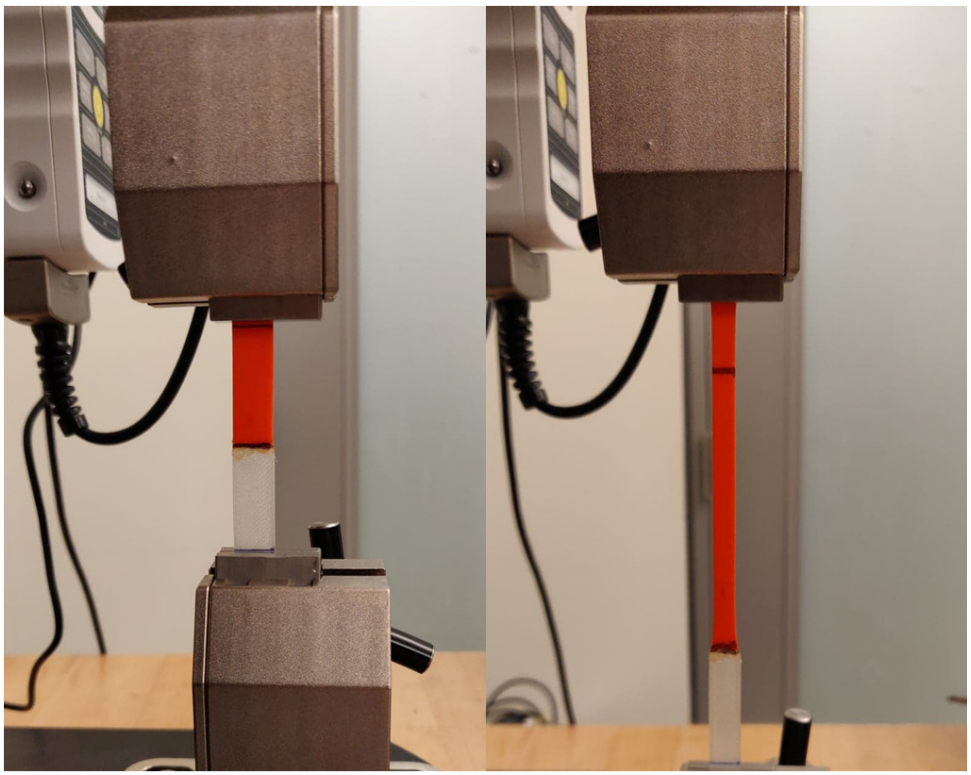

FIGURE 5.8: Experimental set-up for multi-material tensile test. The gauge length of each material is 20mm; NinjaFlex in orange, Cheetah in white.

to show the effects of hyperelastic properties on a mesh of 500 elements. The first with linear behaviour using the tangent modulus at rest. The second test used the polynomial material curves outlined earlier. The simulation results of both linear and hyperelastic materials are depicted in Fig. 5.10. A clearer picture can be seen of non-linear material properties when observing Fig. 5.9, where the strain of the hyperelastic Cheetah seems to be on an up-turn near the end, and the trend of the hyperelastic NinjaFlex is on a down-turn. This signifies the NinjaFlex is at a point of stiffening in its material curve, while the Cheetah's stiffness is relaxing. Compared to the linear simulation, where there is no change throughout the deformation. This kind of interaction becomes all the more prevalent as the number of materials increase. This leads to potentially drastic different configurations for soft robots compared to linear material modelling. This will change the final positioning but also the path the robot will follow.

From Table 5.2, the difference between the hyperelastic simulation and the experiment is only -1.3% in terms of the location of the material joint, the linear simulation

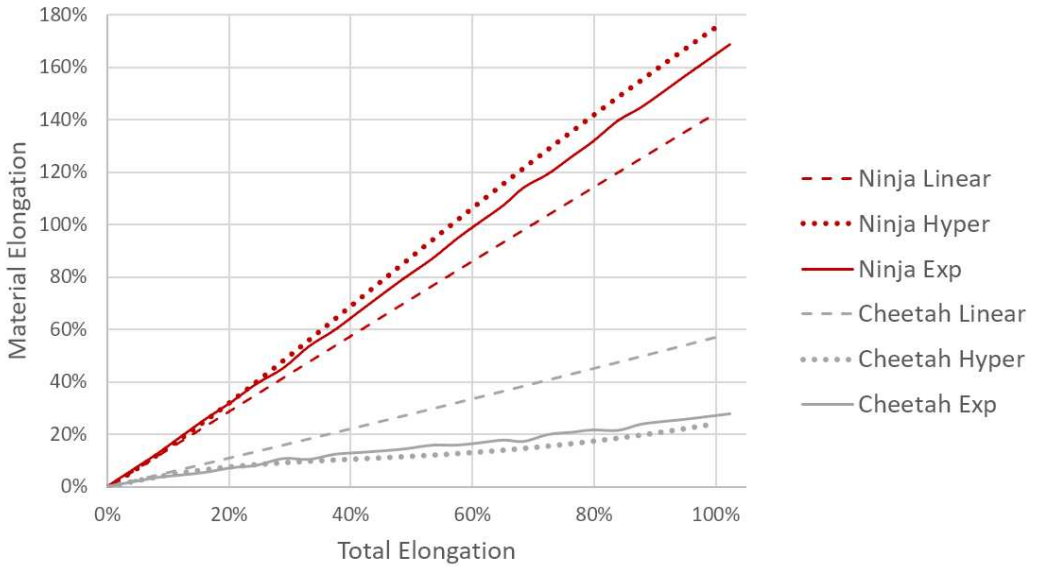

FIGURE 5.9: Graphical representation of the multi-material hyperelastic tensile test. Red depicts NinjaFlex, gray is cheetah.

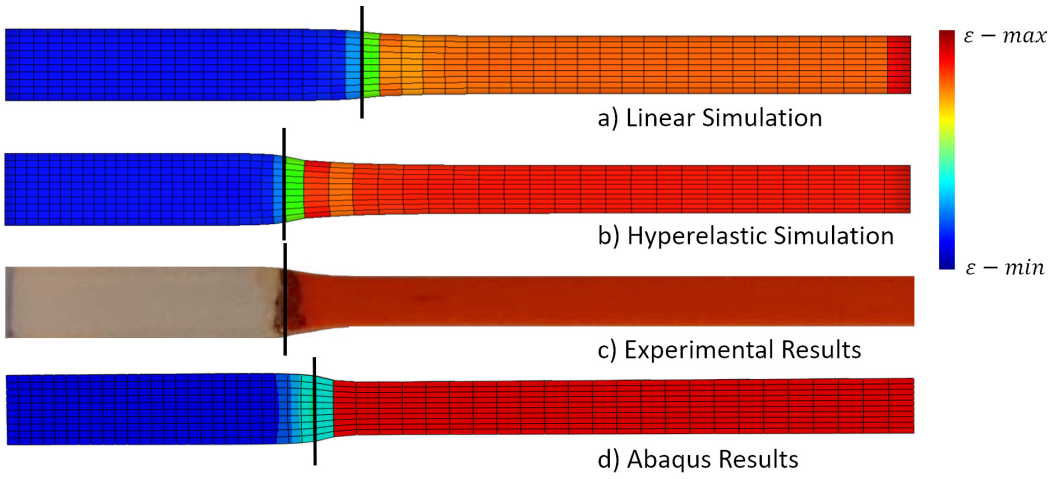

FIGURE 5.10: Cheetah(white) and NinjaFlex(orange) filaments in tension at 100% elongation. a)Linear simulation of my framework; b) Hyperelastic simulation in my framework; c) Experimental results; d) Hyperelastic Abaqus results.

Table 5.2: Comparison of Multi-Material Tensile Test

Tests	Position (Error)	Cheetah Strain (Error)	NinjaFlex Strain (Error)
Experimental	31.5%	26.8%	168.8%
Linear Sim	39.5% (25.4%)	56.9% (112.3%)	142.3.8% (-15.7%)
Hyperelastic Sim	31.1% (-1.3%)	23.9% (-10.8%)	174.8% (3.6%)
Abaqus Hyper	34.7% (11.6%)	38.8% (62.3%)	161.2% (-7.8%)

shows a difference of 25.4%. When looking at individual strain, the difference for Cheetah is -10.8%, while the linear simulation shows an error of 112.3%. This can be explained by the quick softening of the NinjaFlex relative to the Cheetah, illustrating the non-linear behaviour. When comparing to the experimental results, Abaqus performed worse than my framework. Through simulating this experiment on Abaqus, it was clear that the interface between materials became problematic when large deformations occurred. Abaqus took 27.2 seconds for the simulation, while my framework took 18.3 seconds. A 1.49x speed increase is observed. However, the error for Abaqus is 11.6% compared to -1.3% for my method.

5.5 Conclusion

This chapter has formulated a novel method for characterizing non-linear and hyperelastic material properties to a geometry-based approach. In this method, material properties can directly and efficiently be integrated into a local shape blending technique dynamically with negligible performance decrease. The calibration for multiple materials was done based on the equivalent strain energy experienced during uni-axial tensile tests. As such, a direct relation with the mechanical properties of the material could be established and used in the geometry framework. This allowed for a more complete understanding and selection of the shape factor, enabling the direct implementation of material curves. Through the multi-material tensile test, 3D printed specimen were deformed and fitted to obtain material properties. These were compared to a linear model and demonstrated significant differences in results between the two. This further highlights the need for non-linear models for 3D printed filaments and their incorporation in simulation. Compared with standard FEA, the rotational

test also showed agreeable results while still maintaining previous performance benchmarks established by the geometry-based approach.

Chapter 6

Conclusion

Soft robotic grippers have potential to significantly improve automation in industries requiring adaptability, compliance, and safe human interaction. However, their widespread adoption has been hindered by challenges in modelling, design, and simulation—particularly in tendon-driven systems, where the interaction between cables and elastic surfaces introduces complex, nonlinear behaviours. This thesis helps address these limitations by contributing a new formulation for cable friction, a gripper design framework, and improving simulation accuracy, providing a foundation for more efficient and predictable soft robotic systems. By bridging gaps between fundamental research and practical implementation, these advancements are a meaningful step forward for standardized, repeatable, and scalable design processes, bringing tendon-driven soft robots closer to widespread adoption.

Cable friction has been heavily researched for over a century. However, only relatively recently have applications been found where elastic cables interact with elastic surfaces. This thesis contributes to the understanding of this interaction by proposing a friction formulation that also accounts for the asperity behaviour of the friction surface. Additionally, a new experimental methodology is introduced to efficiently determine the friction coefficient for soft robotic systems with minimal data, significantly reducing the reliance on time-consuming physical testing.

Building on this foundation, a structured design pipeline for tendon-driven soft robotic grippers is developed. The second component of this thesis focuses on efficiently narrowing the gripper design space by introducing a grasp-based product mix concept, which categorizes food products based on their required grasp type. This classification enhances adaptability in food automation by reducing the need for

frequent gripper reconfiguration. With a more focused design domain, a streamlined development pipeline is proposed, integrating human demonstration data, grasp strategy optimization, and kinematic modelling. This approach significantly reduces both development time and cost while ensuring that the resulting grippers remain effective across a range of handling tasks. Finally, an optimization framework is introduced to further enhance gripper performance by incorporating hyperelastic material properties, optimizing cable routing paths, and tuning joint stiffness. These refinements minimize actuation force requirements while improving grasp stability and overall efficiency.

The final component of my thesis extends the current state-of-the-art simulation framework for soft robots by formulating an efficient computation scheme for incorporating hyper-elasticity within a geometric representation. This approach ensures that the global stiffness matrix remains constant throughout the simulation, preserving computational efficiency while accurately capturing nonlinear material behaviour. A mathematical model is established to define and calibrate the relationship between shape factors and material properties, enabling stiffness to be represented as a geometric quantity. By evaluating the strain energy of each deformation element, the framework dynamically determines instantaneous stiffness values and updates the corresponding shape factors at each step. As a result, the method remains applicable across an effectively infinite range of materials.

This thesis has taken significant steps toward solving fundamental challenges in tendon-driven soft robotics, providing new methodologies that improve friction modelling, streamline gripper design, and enhance simulation accuracy. Yet, these contributions are only the beginning. The future of soft robotics promises to be one of interdisciplinary innovation—where mechanics, materials science, artificial intelligence, and bio-inspired engineering converge to create machines that are more adaptable, efficient, and intelligent than ever before. The journey ahead is filled with open questions, but each one presents an opportunity to push the boundaries of what soft robotics can achieve.

6.1 Future Work

The contributions of this thesis lay a strong foundation for future research, opening up several exciting directions that can deepen our understanding and expand the capabilities of tendon-driven soft robotic grippers.

The friction model developed in this thesis has proven effective in capturing the behaviour of elastic cables interacting with elastic surfaces under typical conditions found in tendon-driven soft robots. Future research can extend this model to incorporate actuation speed as a parameter while expanding the range of tested loads and angles. As soft robotic materials allow for significant deformation under tension, an increase in frictional contact area could lead to a more nuanced model—potentially drawing inspiration from V-belt friction mechanics. Additionally, improvements in the experimental setup, such as more sensitive measurement devices, could enhance visualization of the stick-slip transition, providing deeper insight into frictional dynamics. Another crucial direction is the study of cyclic loading, as repeated actuation and relaxation may alter internal friction forces over time, affecting the robot's long-term performance and deformation path. Furthermore, real-world industrial applications will introduce wear on soft surfaces, reducing asperity effects and changing friction coefficients.

The gripper design methodology established in this thesis provides a streamlined approach to transferring human grasping strategies into soft robotic systems, significantly improving design efficiency. Future work can enhance the gripper design by incorporating textured gripping surfaces or silicone-based friction coatings to improve contact stability. Another promising avenue is optimizing grasping synergies across all fingers, ensuring coordinated actuation that minimizes the number of actuators required while preserving dexterity. Further refining the thumb's capabilities—through additional degrees of freedom, variable stiffness tuning, or multi-actuation configurations could dramatically expand the range of feasible grasps, making soft robotic hands even more adaptable for complex manipulation tasks.

The simulation framework presented in this thesis introduces a novel approach to representing hyperelastic materials through a geometric shape factor, enabling accurate simulations without the computational burden of continuously updating the

global stiffness matrix. This technique can be extended in several ways. First, introducing multiple local stiffness metrics could better capture complex, multi-directional loading scenarios. Further refinement could incorporate anisotropic effects, temperature-dependent behaviour, and strain rate considerations. Another exciting direction is integrating 3D-printed metamaterials and lattice structures into the framework, treating them as tunable digital materials whose stiffness and deformation properties can be algorithmically optimized. The speed of my simulation framework could be leveraged to allow for rapid, performance-driven material distribution and topology optimization. Additionally, existing research on digital material formulations [104] suggests the potential for real-time iterative updates to material properties, which could be seamlessly integrated into this framework for adaptive soft robotic systems that adjust their properties dynamically based on external forces and operational conditions.

Bibliography

[1] Anthony L Gunderman, Jeremy A Collins, Andrea L Myers, Renee T Threlfall, and Yue Chen. Tendon-driven soft robotic gripper for blackberry harvesting. *IEEE Robotics and Automation Letters*, 7(2):2652–2659, 2022.

[2] Steffen Puhlmann, Jason Harris, and Oliver Brock. Rbo hand 3: A platform for soft dexterous manipulation. *IEEE Transactions on Robotics*, 38(6):3434–3449, 2022.

[3] Alireza Mohammadi, Jim Lavranos, Hao Zhou, Rahim Mutlu, Gursel Alici, Ying Tan, Peter Choong, and Denny Oetomo. A practical 3d-printed soft robotic prosthetic hand with multi-articulating capabilities. *PloS one*, 15(5):e0232766, 2020.

[4] Yuxuan Liu, Jixin Hou, Changying Li, and Xianqiao Wang. Intelligent soft robotic grippers for agricultural and food product handling: A brief review with a focus on design and control. *Advanced Intelligent Systems*, 5(12):2300233, 2023.

[5] Lillian Chin, Jeffrey Lipton, Michelle C Yuen, Rebecca Kramer-Bottiglio, and Daniela Rus. Automated recycling separation enabled by soft robotic material classification. In *2019 2nd IEEE International Conference on Soft Robotics (RoboSoft)*, pages 102–107. IEEE, 2019.

[6] Matteo Cianchetti, Cecilia Laschi, Arianna Menciassi, and Paolo Dario. Biomedical applications of soft robotics. *Nature Reviews Materials*, 3:143–153, 2018.

[7] Jonathan Rossiter, B. Stoimenov, and Andrew Conn. Biomimetic soft robotics: Progress and challenges. *International Journal of Robotics Research*, 31(13):1628–1645, 2012.

[8] Yuzhe Wang, Zhen Xie, Huishi Huang, and Xinquan Liang. Pioneering healthcare with soft robotic devices: A review. *Smart Medicine*, page e20230045, 2024.

[9] Guoxin Fang, Christopher-Denny Matte, Rob BN Scharff, Tsz-Ho Kwok, and Charlie CL Wang. Kinematics of soft robots by geometric computing. *IEEE Transactions on Robotics*, 36(4):1272–1286, 2020.

[10] Daekyum Kim, Sang-Hun Kim, Taekyoung Kim, Brian Byunghyun Kang, Minhyuk Lee, Wookeun Park, Subyeong Ku, DongWook Kim, Junghan Kwon, Hochang Lee, et al. Review of machine learning methods in soft robotics. *Plos one*, 16(2):e0246102, 2021.

[11] Guo Liang Goh, Xi Huang, William Toh, Zhengchen Li, Samuel Lee, Wai Yee Yeong, Boon Siew Han, Teng Yong Ng, et al. Joint angle prediction for a cable-driven gripper with variable joint stiffness through numerical modeling and machine learning. *International Journal of AI for Materials and Design*, 1(1):2328, 2024.

[12] Gionata Salvietti, Irfan Hussain, Monica Malvezzi, and Domenico Prattichizzo. Design of the passive joints of underactuated modular soft hands for fingertip trajectory tracking. *IEEE Robotics and Automation Letters*, 2(4):2008–2015, 2017.

[13] Rajarshi Roy, Long Wang, and Nabil Simaan. Modeling and estimation of friction, extension, and coupling effects in multisegment continuum robots. *IEEE/ASME Transactions on Mechatronics*, 22(2):909–920, 2016.

[14] Dongyang Chen, Youngmok Yun, and Ashish D Deshpande. Experimental characterization of bowden cable friction. In *2014 IEEE international conference on robotics and automation (ICRA)*, pages 5927–5933. IEEE, 2014.

[15] Werner Kraus, Michael Kessler, and Andreas Pott. Pulley friction compensation for winch-integrated cable force measurement and verification on a cable-driven parallel robot. In *2015 IEEE International Conference on Robotics and Automation (ICRA)*, pages 1627–1632. IEEE, 2015.

[16] Eulalie Coevoet, Thor Morales-Bieze, Frederick Largilliere, Zhongkai Zhang, Maxime Thieffry, Mario Sanz-Lopez, Bruno Carrez, Damien Marchal, Olivier Goury, Jeremie Dequidt, et al. Software toolkit for modeling, simulation, and control of soft robots. *Advanced Robotics*, 31(22):1208–1224, 2017.

[17] Keiji Imado and T Ghrib. Frictional property of flexible element. *New Tribological Ways*, pages 235–264, 2011.

[18] Robert C Juvinall and Kurt M Marshek. *Fundamentals of machine component design*. John Wiley & Sons, 2020.

[19] Vlado A Lubarda. The mechanics of belt friction revisited. *International Journal of Mechanical Engineering Education*, 42(2):97–112, 2014.

[20] William E Heap, Chris T Keeley, Elvy B Yao, Nicholas D Naclerio, and Elliot W Hawkes. Miniature, lightweight, high-force, capstan winch for mobile robots. *IEEE Robotics and Automation Letters*, 7(4):9873–9880, 2022.

[21] Soft-Gripping. https://www.soft-gripping.shop/en/. [Accessed 18-09-2024].

[22] Thomas Feix, Javier Romero, Heinz-Bodo Schmiedmayer, Aaron M. Dollar, and Danica Kragic. The grasp taxonomy of human grasp types. *IEEE Transactions on Human-Machine Systems*, 46(1):66–77, 2016.

[23] Angus B Clark, Lois Liow, and Nicolas Rojas. Force evaluation of tendon routing for underactuated grasping. *Journal of Mechanical Design*, 143(10):104502, 2021.

[24] Tiantian Liu, Sofien Bouaziz, and Ladislav Kavan. Quasi-newton methods for real-time simulation of hyperelastic materials. *ACM Trans. Graph.*, 36(4), 2017.

[25] Christian Duriez, E Coevoet, F Largilliere, T Morales-Bieze, Z Zhang, M Sanz-Lopez, B Carrez, Damien Marchal, Olivier Goury, and J Dequidt. Framework for online simulation of soft robots with optimization-based inverse model. *in IEEE Int. Conf. on Simulation, Modeling, and Programming for Autonomous Robots*, pages 111–118, 12 2016.

[26] Jonathan D. Hiller and Hod Lipson. Dynamic simulation of soft heterogeneous objects. *CoRR*, abs/1212.2845, 2012.

[27] Jean Chenevier, David González, J. Vicente Aguado, Francisco Chinesta, and Elías Cueto. Reduced-order modeling of soft robots. *PLOS ONE*, 13(2):1–15, 02 2018.

[28] Jan Bender, Matthias Müller, Miguel A. Otaduy, Matthias Teschner, and Miles Macklin. A survey on position-based simulation methods in computer graphics. *Comput. Graph. Forum*, 33(6):228–251, September 2014.

[29] Tsz-Ho Kwok and Yong Chen. Geometry-driven finite element for four-dimensional printing. *Journal of Manufacturing Science and Engineering*, 07 2017.

[30] G. Fang, C. Matte, R. B. N. Scharff, T. Kwok, and C. C. L. Wang. Kinematics of soft robots by geometric computing. *IEEE Transactions on Robotics*, 36(4):1272–1286, 2020.

[31] Nicholas W. Bartlett, Michael T. Tolley, Johannes T. B. Overvelde, James C. Weaver, Bobak Mosadegh, Katia Bertoldi, George M. Whitesides, and Robert J. Wood. A 3d-printed, functionally graded soft robot powered by combustion. *Science*, 349(6244):161–165, 2015.

[32] Odhner Lael U. and Ma Raymond R.and Dollar Aaron M. *Experiments in Underactuated In-Hand Manipulation*, volume 88, pages 27–40. Springer International Publishing, Heidelberg, 2013.

[33] M. Tavakoli and A. T. de Almeida. Adaptive under-actuated anthropomorphic hand: Isr-softhand. In *IEEE/RSJ International Conference on Intelligent Robots and Systems*, pages 1629–1634, Sept 2014.

[34] François Schmitt, Olivier Piccin, Laurent Barbé, and Bernard Bayle. Soft robots manufacturing: A review. *Frontiers in Robotics and AI*, 5:84, 2018.

[35] Nahid Elyasi, Kimia Karimi Taheri, Keivan Narooei, and Ali Karimi Taheri. A study of hyperelastic models for predicting the mechanical behavior of extensor

apparatus. *Biomechanics and Modeling in Mechanobiology*, 16(3):1077–1093, Jun 2017.

[36] François Faure, Christian Duriez, Hervé Delingette, Jérémie Allard, Benjamin Gilles, Stéphanie Marchesseau, Hugo Talbot, Hadrien Courtecuisse, Guillaume Bousquet, Igor Peterlik, and Stéphane Cotin. *SOFA: A Multi-Model Framework for Interactive Physical Simulation*, pages 283–321. Springer Berlin Heidelberg, Berlin, Heidelberg, 2012.

[37] Frank Philip Bowden and David Tabor. *The friction and lubrication of solids*, volume 1. Oxford university press, 2001.

[38] Frank Philip Bowden and JE Young. Friction of diamond, graphite, and carbon and the influence of surface films. *Proceedings of the Royal Society of London. Series A. Mathematical and Physical Sciences*, 208(1095):444–455, 1951.

[39] HG Howell. 24—the general case of friction of a string round a cylinder. *Journal of the Textile Institute Transactions*, 44(8-9):T359–T362, 1953.

[40] Jae Ho Jung, Ning Pan, and Tae Jin Kang. Generalized capstan problem: Bending rigidity, nonlinear friction, and extensibility effect. *Tribology International*, 41(6):524–534, 2008.

[41] Jae Ho Jung, Ning Pan, and Tae Jin Kang. Capstan equation including bending rigidity and non-linear frictional behavior. *Mechanism and Machine Theory*, 43(6):661–675, 2008.

[42] D3108 ASTM. Standard test method for coefficient of friction, yarn to solid material, 2020.

[43] Lionel Birglen, Thierry Laliberté, and Clément M Gosselin. *Underactuated robotic hands*, volume 40. Springer, 2007.

[44] Zhen Zhou, Xudong Zheng, Zhang Chen, Xueqian Wang, Bin Liang, and Qi Wang. Dynamics modeling and analysis of cable-driven segmented manipulator considering friction effects. *Mechanism and Machine Theory*, 169:104633, 2022.

[45] Christopher-Denny Matte and Tsz-Ho Kwok. Simulation of hyperelasticity by shape estimation. *Journal of Computing and Information Science in Engineering*, 21(5):050903, 05 2021.

[46] Khaled Elgeneidy, Peter Lightbody, Simon Pearson, and Gerhard Neumann. Characterising 3d-printed soft fin ray robotic fingers with layer jamming capability for delicate grasping. In *2019 2nd IEEE International Conference on Soft Robotics (RoboSoft)*, pages 143–148. IEEE, 2019.

[47] Zhenyu Wan, Yinan Sun, Yun Qin, Erik H Skorina, Renato Gasoto, Ming Luo, Jie Fu, and Cagdas D Onal. Design, analysis, and real-time simulation of a 3d soft robotic snake. *Soft Robotics*, 10(2):258–268, 2023.

[48] Yilun Sun, Yuqing Liu, Nandi Zhou, and Tim C Lueth. A matlab-based framework for designing 3d topology optimized soft robotic grippers. In *2021 IEEE/ASME International Conference on Advanced Intelligent Mechatronics (AIM)*, pages 1283–1289. IEEE, 2021.

[49] JM Fee and DJ Quist. A new cable pulling friction measurement method and results. *IEEE transactions on power delivery*, 7(2):681–686, 1992.

[50] Dang Vu Hung, Joris Degrieck, Lieva Van Langenhove, and Paul Kiekens. Numerical simulation of the yarn-object interaction. *Textile research journal*, 72(8):657–662, 2002.

[51] Anindya Ghosh, Asis Patanaik, RD Anandjiwala, and RS Rengasamy. A study on dynamic friction of different spun yarns. *Journal of applied polymer science*, 108(5):3233–3238, 2008.

[52] SS Ramkumar, Ranjeet Rajanala, S Parameswaran, Robert Paige, A Shaw, DC Shelly, TA Anderson, GP Cobb, R Mahmud, C Roedel, et al. Experimental verification of failure of amontons' law in polymeric textiles. *Journal of applied polymer science*, 91(6):3879–3885, 2004.

[53] Dale J Podolsky, Eric Diller, David M Fisher, Karen W Wong Riff, Thomas Looi, James M Drake, and Christopher R Forrest. Utilization of cable guide

channels for compact articulation within a dexterous three degrees-of-freedom surgical wrist design. *Journal of Medical Devices*, 13(1):011003, 2019.

[54] Yuxuan Liu, Jixin Hou, Changying Li, and Xianqiao Wang. Intelligent soft robotic grippers for agricultural and food product handling: A brief review with a focus on design and control. *Advanced Intelligent Systems*, 5(12):2300233, 2023.

[55] TK Lien. Gripper technologies for food industry robots. In *Robotics and automation in the food industry*, pages 143–170. Elsevier, 2013.

[56] Zhongkui Wang, Keung Or, and Shinichi Hirai. A dual-mode soft gripper for food packaging. *Robotics and Autonomous Systems*, 125:103427, 2020.

[57] Yufei Hao, Shantonu Biswas, Elliot Wright Hawkes, Tianmiao Wang, Mengjia Zhu, Li Wen, and Yon Visell. A multimodal, enveloping soft gripper: Shape conformation, bioinspired adhesion, and expansion-driven suction. *IEEE Transactions on Robotics*, 37(2):350–362, 2020.

[58] Ping Zhang, Weichun Chen, and Bin Tang. Design and feasibility tests of a lightweight soft gripper for compliant and flexible envelope grasping. *Soft Robotics*, 9(2):376–385, 2022.

[59] Finger gripper mGrip — schmalz.com. https://www.schmalz.com/en-ca/vacuum-technology-for-automation/vacuum-components/area-gripping-systems-and-end-effectors/finger-grippers/finger-gripper-mgrip/. [Accessed 18-09-2024].

[60] ROCHU | China Best Soft Robotics Gripper Solutions. https://www.softroboticgripper.com/. [Accessed 18-09-2024].

[61] Hongying Zhang, A Senthil Kumar, Feifei Chen, Jerry YH Fuh, and Michael Yu Wang. Topology optimized multimaterial soft fingers for applications on grippers, rehabilitation, and artificial hands. *IEEE/ASME Transactions on Mechatronics*, 24(1):120–131, 2018.

[62] Baohua Zhang, Yuanxin Xie, Jun Zhou, Kai Wang, and Zhen Zhang. State-of-the-art robotic grippers, grasping and control strategies, as well as their applications in agricultural robots: A review. *Computers and Electronics in Agriculture*, 177:105694, 2020.

[63] Yafeng Cui, Xin-Jun Liu, Xuguang Dong, Jingyi Zhou, and Huichan Zhao. Enhancing the universality of a pneumatic gripper via continuously adjustable initial grasp postures. *IEEE Transactions on Robotics*, 37(5):1604–1618, 2021.

[64] Gen Endo and Nobuhiro Otomo. Development of a food handling gripper considering an appetizing presentation. In *2016 IEEE International Conference on Robotics and Automation (ICRA)*, pages 4901–4906. IEEE, 2016.

[65] A Pettersson, Thomas Ohlsson, S Davis, JO Gray, and TJ Dodd. A hygienically designed force gripper for flexible handling of variable and easily damaged natural food products. *Innovative Food Science & Emerging Technologies*, 12(3):344–351, 2011.

[66] Irfan Hussain, Oraib Al-Ketan, Federico Renda, Monica Malvezzi, Domenico Prattichizzo, Lakmal Seneviratne, Rashid K Abu Al-Rub, and Dongming Gan. Design and prototyping soft–rigid tendon-driven modular grippers using interpenetrating phase composites materials. *The International Journal of Robotics Research*, 39(14):1635–1646, 2020.

[67] Rahim Mutlu, Gursel Alici, Marc in het Panhuis, and Geoff Spinks. Effect of flexure hinge type on a 3d printed fully compliant prosthetic finger. In *2015 IEEE International Conference on Advanced Intelligent Mechatronics (AIM)*, pages 790–795. IEEE, 2015.

[68] Bin Fang, Fuchun Sun, Linyuan Wu, Fukang Liu, Xiangxiang Wang, Haiming Huang, Wenbing Huang, Huaping Liu, and Li Wen. Multimode grasping soft gripper achieved by layer jamming structure and tendon-driven mechanism. *Soft Robotics*, 9(2):233–249, 2022.

[69] Charbel Tawk, Rahim Mutlu, and Gursel Alici. A 3d printed modular soft gripper integrated with metamaterials for conformal grasping. *Frontiers in Robotics and AI*, 8:799230, 2022.

[70] Chih-Hsing Liu, Yi-Chieh Shih, and Jui-Chih Chi. Topology optimization and prototype of a highly adaptive multi-material compliant finger for parallel grippers. *IEEE Robotics and Automation Letters*, 2024.

[71] Christopher-Denny Matte and Tsz Ho Kwok. Modeling elastic cable-surface friction for soft robots. *Journal of Computing and Information Science in Engineering*, pages 1–13, 2024.

[72] Fionnuala Connolly, Conor J Walsh, and Katia Bertoldi. Automatic design of fiber-reinforced soft actuators for trajectory matching. *Proceedings of the National Academy of Sciences*, 114(1):51–56, 2017.

[73] Xiaodong Li, Rongwei Wen, Dehao Duanmu, Wei Huang, Kinto Wan, and Yong Hu. Finger kinematics during human hand grip and release. *Biomimetics*, 8(2):244, 2023.

[74] Jan Fras and Kaspar Althoefer. Soft biomimetic prosthetic hand: Design, manufacturing and preliminary examination. In *2018 IEEE/RSJ international conference on intelligent robots and systems (IROS)*, pages 1–6. IEEE, 2018.

[75] Revanth Konda, David Bombara, Steven Swanbeck, and Jun Zhang. Anthropomorphic twisted string-actuated soft robotic gripper with tendon-based stiffening. *IEEE Transactions on Robotics*, 39(2):1178–1195, 2022.

[76] Charbel Tawk, Hao Zhou, Emre Sariyildiz, Marc In Het Panhuis, Geoffrey M Spinks, and Gursel Alici. Design, modeling, and control of a 3d printed monolithic soft robotic finger with embedded pneumatic sensing chambers. *IEEE/ASME Transactions on Mechatronics*, 26(2):876–887, 2020.

[77] Hao Zhou, Charbel Tawk, and Gursel Alici. A 3d printed soft robotic hand with embedded soft sensors for direct transition between hand gestures and improved grasping quality and diversity. *IEEE Transactions on Neural Systems and Rehabilitation Engineering*, 30:550–558, 2022.

[78] Lisha Chen, Chenghao Yang, Hua Wang, David T. Branson, Jian S. Dai, and Rongjie Kang. Design and modeling of a soft robotic surface with hyperelastic material. *Mechanism and Machine Theory*, 130:109 – 122, 2018.

[79] H. Zhang, A. S. Kumar, J. Y. H. Fuh, and M. Y. Wang. Topology optimized design, fabrication and evaluation of a multimaterial soft gripper. In *2018 IEEE International Conference on Soft Robotics (RoboSoft)*, pages 424–430, 2018.

[80] F. Largilliere, V. Verona, E. Coevoet, M. Sanz-Lopez, J. Dequidt, and C. Duriez. Real-time control of soft-robots using asynchronous finite element modeling. In *2015 IEEE International Conference on Robotics and Automation (ICRA)*, pages 2550–2555, May 2015.

[81] Nick Cheney, Robert MacCurdy, Jeff Clune, and Hod Lipson. Unshackling evolution: Evolving soft robots with multiple materials and a powerful generative encoding. In *GECCO 2013 - Proceedings of the 2013 Genetic and Evolutionary Computation Conference*, 01 2013.

[82] François Goulette and Zhuo-Wei Chen. Fast computation of soft tissue deformations in real-time simulation with hyper-elastic mass links. *Computer Methods in Applied Mechanics and Engineering*, 295:18 – 38, 2015.

[83] Christopher Brandt, Elmar Eisemann, and Klaus Hildebrandt. Hyper-reduced projective dynamics. *ACM Trans. Graph.*, 37(4):80:1–80:13, July 2018.

[84] Hongyi Xu, Funshing Sin, Yufeng Zhu, and Jernej Barbič. Nonlinear material design using principal stretches. *ACM Trans. on Graphics (SIGGRAPH 2015)*, 34(4), 2015.

[85] Breannan Smith, Fernando De Goes, and Theodore Kim. Stable neo-hookean flesh simulation. *ACM Trans. Graph.*, 37(2):12:1–12:15, 2018.

[86] Andrea Mendizabal, Pablo Márquez-Neila, and Stéphane Cotin. Simulation of hyperelastic materials in real-time using deep learning. *Medical Image Analysis*, 59:101569, 2020.

[87] Matthias Müller, Bruno Heidelberger, Marcus Hennix, and John Ratcliff. Position based dynamics. *J. Vis. Commun. Image Represent*, 18(2):109 – 118, 2007.

[88] M. Shapira and A. Rappoport. Shape blending using the star-skeleton representation. *IEEE Computer Graphics and Applications*, 15(2):44–50, March 1995.

[89] Olga Sorkine and Marc Alexa. As-rigid-as-possible surface modeling. In *Proceedings of the Fifth Eurographics Symposium on Geometry Processing*, SGP '07, pages 109–116, Aire-la-Ville, Switzerland, Switzerland, 2007. Eurographics Association.

[90] Shuo Jin, Yunbo Zhang, and Charlie C.L. Wang. Deformation with enforced metrics on length, area and volume. *Computer Graphics Forum*, 33(2):429–438, 2014.

[91] Ligang Liu, Lei Zhang, Yin Xu, Craig Gotsman, and Steven J. Gortler. A local/global approach to mesh parameterization. In *Proceedings of the Symposium on Geometry Processing*, SGP '08, pages 1495–1504, Aire-la-Ville, Switzerland, Switzerland, 2008. Eurographics Association.

[92] Sofien Bouaziz, Mario Deuss, Yuliy Schwartzburg, Thibaut Weise, and Mark Pauly. Shape-up: Shaping discrete geometry with projections. *Comput. Graph. Forum*, 31(5):1657–1667, 2012.

[93] Lionel Birglen, Thierry Laliberté, and Clément M Gosselin. *Underactuated robotic hands*, volume 40. Springer, 2007.

[94] Shima Akhondi, Christopher-Denny Matte, and Tsz Ho Kwok. A study on mechanical behavior of 3d printed elastomers with various infills and densities. *Manufacturing Letters*, 35:592–602, 2023.

[95] JF Archard. Elastic deformation and the laws of friction. *Proceedings of the royal society of London. Series A. Mathematical and physical sciences*, 243(1233):190–205, 1957.

[96] Hao Zhou, Alireza Mohammadi, Denny Oetomo, and Gursel Alici. A novel monolithic soft robotic thumb for an anthropomorphic prosthetic hand. *IEEE Robotics and Automation Letters*, 4(2):602–609, 2019.

[97] Camillo Lugaresi, Jiuqiang Tang, Hadon Nash, Chris McClanahan, Esha Uboweja, Michael Hays, Fan Zhang, Chuo-Ling Chang, Ming Guang Yong, Juhyun Lee, Wan-Teh Chang, Wei Hua, Manfred Georg, and Matthias Grundmann. Mediapipe: A framework for building perception pipelines, 2019.

[98] T. H. Kwok, W. Wan, J. Pan, C. C. L. Wang, J. Yuan, K. Harada, and Y. Chen. Rope caging and grasping. In *IEEE International Conference on Robotics and Automation (ICRA)*, pages 1980–1986, sgsiog, May 2016.

[99] H. Khajehsaeid, J. Arghavani, and R. Naghdabadi. A hyperelastic constitutive model for rubber-like materials. *European Journal of Mechanics - A/Solids*, 38:144 – 151, 2013.

[100] Christine Renaud, Jean-Michel Cros, Zhi-Qiang Feng, and Bintang Yang. The yeoh model applied to the modeling of large deformation contact/impact problems. *International Journal of Impact Engineering*, 36(5):659 – 666, 2009.

[101] Isaac Chao, Ulrich Pinkall, Patrick Sanan, and Peter Schröder. A simple geometric model for elastic deformations. *ACM Trans. Graph.*, 29(4), July 2010.

[102] Gaël Guennebaud, Benoît Jacob, et al. Eigen v3. http://eigen.tuxfamily.org, 2010.

[103] R. W. Ogden. Large deformation isotropic elasticity - on the correlation of theory and experiment for incompressible rubberlike solids. *Proceedings of the Royal Society of London. Series A, Mathematical and Physical Sciences*, 326(1567):565–584, 1972.

[104] Yuen-Shan Leung, Tsz-Ho Kwok, Huachao Mao, and Yong Chen. Digital material design using tensor-based error diffusion for additive manufacturing. *Computer-Aided Design*, 114:224 – 235, 2019.